arXiv:2608.08319v1 [cs.CV] 8 Aug 2026

A continually expandable foundation model for brain MRI

Michail Mamalakis, Carmen Jimenez-Mesa, Yonghao Li, Hao Chen, Chao Li, Antonios Mamalakis, John Suckling, Richard Bethlehem, Stephen J. Price, Richard J. Gilbertson, Pietro Lio, *for the Alzheimer's Disease Neuroimaging Initiative*[**]

[1*]Cancer Research UK Cambridge Institute, University of Cambridge Li Ka Shing Centre, Robinson Way, Cambridge, CB2 0RE, Cambridgeshire, United Kingdom.

[2]Department of Computer Science and Technology, University of Cambridge, 15 JJ Thomson Ave, Cambridge, CB3 0FD, Cambridgeshire, United Kingdom.

[3]Department of Psychiatry, University of Cambridge, Hills Road, Cambridge, CB2 2QQ, Cambridgeshire, United Kingdom.

[4]Department of Psychology, University of Cambridge, Downing Pl, Cambridge, CB2 3EB, Cambridgeshire, United Kingdom.

[5]Department of Communication Engineering E.T.S. Ingeniería de Telecomunicación, University of Málaga, Blvd. Louis Pasteur 35, Malaga, 29010, Spain.

[6]Department of Applied Mathematics and Theoretical Physics, University of Cambridge, Wilberforce Rd, Cambridge, CB3 0WA, Cambridgeshire, United Kingdom.

[7]Department of Oncology, University of Cambridge, Cambridge Biomedical Campus, Cambridge, CB2 0SP, Cambridgeshire, United Kingdom.

[8]Department of Clinical Neuroscience, University of Cambridge, Cambridge Biomedical Campus, Cambridge, CB2 0SP, Cambridgeshire, United Kingdom.

[9]School of Data Science, University of Virginia, Charlottesville, VA, United States of America .

[10] DaSCI Andalusian Institute of Data Science and Computational Intelligence,University of Granada, Av. del Conocimiento 37, Granada, 18016, Granada, Spain.

*Corresponding author(s). E-mail(s): mm2703@cam.ac.uk;
Contributing authors: cj473@cam.ac.uk; yl860@cam.ac.uk;
hc666@cam.ac.uk; cl647@cam.ac.uk; npa4tg@virginia.edu;
js369@cam.ac.uk; rb643@cam.ac.uk; sjp58@cam.ac.uk;
Richard.Gilbertson@cruk.cam.ac.uk; pl219@cam.ac.uk;

**Data used in preparation of this article were obtained from the Alzheimer's Disease Neuroimaging Initiative (ADNI) database (https://adni.loni.usc.edu). As such, the investigators within the ADNI contributed to the design and implementation of ADNI and/or provided data but did not participate in the analysis or writing of this report. A complete listing of ADNI investigators can be found at https://adni.loni.usc.edu/wp-content/uploads/how_to_apply/ADNI_Acknowledgement_List.pdf.

Brain magnetic resonance imaging (MRI) is central to neuroscience and clinical assessment, but models are commonly developed for individual diseases, populations or imaging protocols. Foundation models promise more general representations, yet they are usually pretrained once and can lose earlier capabilities when updated with new data. Here we show that Alcmaeon, a three-dimensional brain MRI foundation model pretrained without manual labels on more than 425,000 volumes and derived imaging maps, can be expanded sequentially across clinical domains. Alcmaeon combines volumetric encoding and latent diffusion generation with Graph-Blueprint Pruning (GBP), which protects network modules important to earlier domains while leaving the remaining capacity trainable. Across expansion from healthy ageing and neurodegeneration to developmental, psychiatric and tumour imaging, GBP showed less forgetting than sequential adaptation and elastic weight consolidation across voxel-level reconstruction measures, with its largest advantage after adaptation to tumour imaging. The blueprints provided an inspectable record of how model capacity was protected and reused. Representations from different model levels supported image synthesis, disease classification, survival modelling and postoperative prediction, although no single representation was optimal for every task. These findings provide a route towards brain MRI foundation models that can grow with emerging data while retaining earlier capabilities.

Magnetic resonance imaging underpins much of modern neuroscience and neurology, yet computational models for brain MRI remain highly fragmented. Most are developed for a particular disease, cohort, imaging modality or acquisition protocol and often transfer poorly when these conditions change. Foundation models offer a possible route towards more general systems by learning reusable representations from large and diverse datasets before being adapted to specific applications. Developing such models for three-dimensional neuroimaging remains challenging, however, because volumetric data are computationally demanding, imaging protocols are heterogeneous and clinically relevant datasets continue to expand.

Recent foundation and self-supervised models have shown that large-scale brain MRI pretraining can support reconstruction, segmentation and clinical prediction [1–5]. These approaches generally follow a static train–then–adapt design: the model is trained once and subsequently probed or fine-tuned for individual applications. In practice, new neuroimaging data arrive progressively as additional populations, diseases, modalities and acquisition protocols become available. Updating a pretrained model with these data can degrade previously acquired capabilities, a problem known as catastrophic forgetting [6]. Regularisation-based continual-learning methods limit changes to important parameters [7, 8], while masking and subnetwork approaches reserve selected components for earlier tasks [9, 10]. How to preserve earlier computational pathways while continuing to expand a large three-dimensional MRI model nevertheless remains unresolved [11].

Here we introduce Alcmaeon[1], a brain MRI foundation-model framework for large-scale self-supervised pretraining, continual domain expansion and downstream adaptation. Alcmaeon is trained without manual labels on more than 425,000 three-dimensional MRI volumes and derived imaging maps spanning population imaging, healthy ageing, neurodegeneration, developmental and psychiatric cohorts, and adult brain tumours. Rather than treating pretraining as a fixed stage, we organise these data as a sequence of clinically and biologically distinct domains and ask whether the model can acquire each new domain while limiting deterioration in capabilities learned from earlier cohorts.

To support continual expansion, we develop Graph-Blueprint Pruning (GBP), a structural-memory mechanism that ranks domain-associated computational modules using activation–gradient salience. Modules selected for earlier domains are added to a cumulative blueprint and protected during subsequent adaptation, whereas the remaining modules remain trainable. Unlike soft parameter regularisation, GBP therefore places a hard structural constraint on selected parts of the model. The resulting blueprints provide an inspectable, stage-specific record of which modules are selected, protected or still available for later learning. Across the evaluated sequence, GBP most consistently reduced forgetting across voxel-wise reconstruction metrics, with its largest advantage arising after adaptation to tumour imaging.

We first examine whether Alcmaeon can be trained stably at volumetric scale and whether reconstruction depends more strongly on model size, latent design or imaging modality. We then evaluate continual expansion across four clinically distinct domains

[1]The model is named after Alcmaeon of Croton; see the 'Acknowledgement of name inspiration' for further details.

and test whether GBP limits deterioration when both the clinical population and input format change.

Finally, we evaluate representations extracted from different components and depths of the model across cross-modal MRI synthesis, neurodegenerative-disease classification, adult glioma survival modelling and postoperative outcome prediction under limited supervision. These benchmarks assess whether different model representations are suited to distinct generative, diagnostic and prognostic objectives, and whether blueprint-protected representations remain useful after continual expansion. Together, our experiments examine whether a brain MRI foundation model can learn sequentially from heterogeneous clinical domains while limiting the deterioration of previously acquired capabilities. More broadly, Alcmaeon provides a framework in which new neuroimaging domains can be incorporated as data become available, without requiring a separate pretrained model for every disease, cohort or imaging protocol.

Alcmaeon: a continually expandable foundation model for brain MRI

Alcmaeon is a self-supervised foundation model trained without manual labels on more than 425,000 three-dimensional brain MRI volumes and derived imaging maps. It is designed to learn shared representations across heterogeneous MRI data and to extend them sequentially as new clinical domains become available. The architecture comprises four principal components (Fig. 1). A three-dimensional Swin Transformer encoder–decoder, termed 3D-SWIN [12–14], reconstructs structural MRI, diffusion-derived images and quantitative imaging maps through a shared latent representation. A volumetric Diffusion Transformer, termed 3D-DiT [15–17], models the distribution of these latent representations and supports image synthesis and cross-modal translation. Task-specific prediction heads connect the learned representations to diagnostic and prognostic endpoints. Finally, Graph-Blueprint Pruning (GBP) ranks domain-associated computational modules and protects selected modules during subsequent adaptation, providing a structural memory of previously learned domains.

The 3D-SWIN reconstruction network adapts the hierarchical shifted-window architecture of SwinUNETR and incorporates U-Net-style skip connections [12, 13, 18]. The 3D-DiT generator operates within the compact bottleneck representation rather than directly in the full-resolution voxel space, reducing the computational cost of volumetric generation and allowing the reconstruction and generative components to share a latent space. GBP maintains separate blueprints for the encoder–decoder and latent generator and can constrain these components independently or jointly. After each domain, modules with high activation–gradient salience are added to the cumulative blueprint and protected during subsequent adaptation, whereas the remaining modules remain trainable. Architectural and implementation details are provided in Methods.

Latent design influences reconstruction more strongly than model scale

Alcmaeon was initially trained through self-supervised reconstruction on UK Biobank, which provided population-scale structural MRI, diffusion MRI and neurite orientation dispersion and density imaging (NODDI)-derived maps from a predominantly healthy population. The model was then expanded sequentially to healthy ageing in D1, neurodegenerative disease in D2, developmental and psychiatric imaging in D3, and adult glioma and brain-tumour imaging in D4. This sequence introduced changes in age distribution, pathology, modality composition and acquisition protocol. Tumour imaging was placed last to test adaptation under a pronounced anatomical and pathological shift while measuring retention of earlier-domain performance. We evaluated four model scales: Small (approximately 33 million parameters), Base (131 million), Large (580 million) and Extra-Large (676 million).

We first examined whether Alcmaeon could be trained stably at volumetric scale and how reconstruction performance varied with optimization configuration, latent design, imaging modality and model size (Extended Data Figs. 1 and 2). Among the evaluated distributed-training configurations, those combining larger global batches with greater hardware parallelism showed smoother optimization trajectories and reached stable reconstruction losses earlier. We selected the configuration with a global batch size of 512 for subsequent experiments. Because batch size and hardware parallelism varied together, this comparison characterizes the complete training configuration rather than an independent effect of batch size. Full optimization analyses are provided in Supplementary Information S9.1.1.

We next tested whether adding latent distribution modelling with 3D-DiT altered the reconstruction fidelity of the deterministic encoder–decoder. Across the evaluated training configurations, 3D-SWIN and 3D-SWIN-DiT differed by no more than approximately 0.1 dB in PSNR and 0.001 in SSIM. Incorporating 3D-DiT was therefore associated with little measurable change in reconstruction fidelity, while its generative performance was assessed separately in the downstream synthesis experiments.

We then compared the deterministic latent representation used by 3D-SWIN-DiT with a variational autoencoder formulation [19]. Their relative reconstruction performance depended on the imaging modality. For diffusion MRI, 3D-SWIN-DiT achieved an SSIM of approximately (0.872), compared with (0.796) for VAE-DiT, and produced lower voxel-wise reconstruction errors. Structural MRI also favoured the non-variational formulation. By contrast, for NODDI-derived microstructural maps, models containing a variational bottleneck achieved an SSIM of approximately (0.888) and reduced voxel-wise errors by more than (30%) relative to the corresponding non-variational model. Thus, deterministic latent representations achieved higher reconstruction fidelity for structural and diffusion MRI, whereas variational regularisation was advantageous for some microstructural maps.

Finally, we examined whether increasing parameter count produced corresponding improvements in reconstruction. Under the evaluated training conditions, gains from the Small to Extra-Large models were modest, and their performance intervals overlapped substantially (Extended Data Fig. 2a–c). By contrast, comparisons between

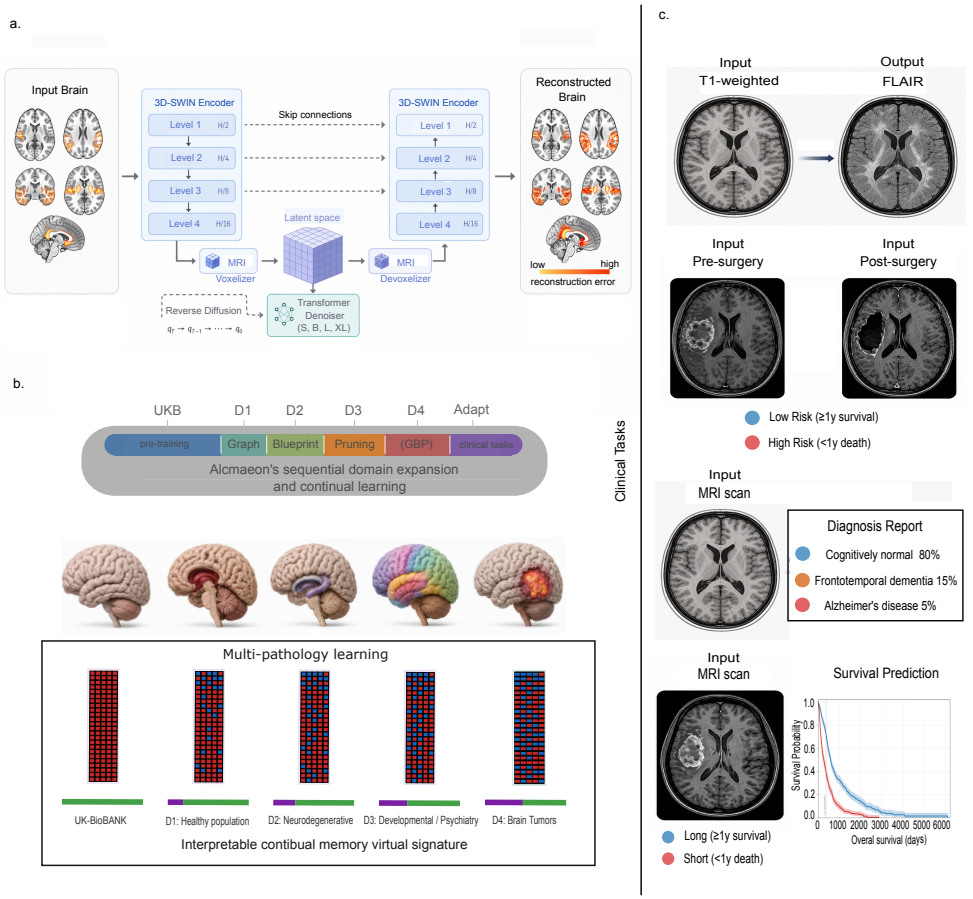


Fig. 1: Alcmaeon is a three-dimensional brain MRI foundation model with Graph-Blueprint continual learning. a. Alcmaeon is trained by reconstructing heterogeneous three-dimensional brain MRI inputs supplied as either paired multimodal channels or pooled single-channel scans. A Swin encoder maps the input volume to a compact latent representation, a transformer denoiser performs reverse diffusion in the latent space, and a devoxeliser and Swin decoder reconstruct the target volume. **b.** Blueprint signatures track how trainable modules are allocated and protected across the sequential trajectory from UK Biobank pretraining to D1 healthy ageing, D2 neurodegeneration, D3 developmental and psychiatric imaging, and D4 adult glioma and brain-tumour imaging. Graph-Blueprint Pruning aggregates activation–gradient module salience, constructs a global blueprint using principal component analysis and protects high-salience modules through a cumulative update rule. Separate blueprints are maintained for the encoder–decoder and latent generator. **c.** Alcmaeon's representations are adapted or evaluated for cross-modal brain-tumour MRI synthesis, neurodegenerative-disease classification, adult glioma survival modelling and post-operative brain-tumour outcome prediction, spanning generative, diagnostic and prognostic applications.

models using the shallower level-2 and deeper level-4 representations showed larger differences associated with latent depth and formulation, particularly for NODDI-derived maps (Extended Data Fig. 1d–f). These results do not establish equivalence among model scales, but they indicate that increasing parameter count alone provided limited gains under the evaluated training conditions.

Together, these analyses show that reliable self-supervised learning across diverse three-dimensional MRI data depended more on how the model encoded the images than on model size alone. Because different types of MRI benefited from different internal representations, we evaluated multiple feature levels and adaptation strategies in the downstream tasks.

Graph-Blueprint Pruning limits forgetting when the clinical domain or input format changes

Adapting across clinical domains and input formats

Continual neuroimaging models must accommodate variation arising from both the clinical population and the structure of the input data. These sources of variation are often confounded because new cohorts may differ simultaneously in disease composition, acquisition protocol and available MRI modalities. We therefore evaluated Alcmaeon under single-channel, two-channel and hybrid input configurations designed to distinguish clinical-domain shift from changes in channel semantics and input dimensionality.

In the single-channel configuration, each MRI volume was processed independently as the model was sequentially adapted to healthy ageing (D1), neurodegeneration (D2), developmental and psychiatric imaging (D3), and adult brain tumours (D4). These domains represent distinct clinical and imaging distributions rather than increasing levels of task complexity. D4 constituted the most disruptive transition because tumour imaging introduced heterogeneous lesions, oedema, mass effect and substantial anatomical distortion. In the two-channel configuration, UK Biobank pretraining used two MRI modalities acquired from the same participant. When consistently paired modalities were unavailable in subsequent domains, the same image was duplicated across the two channels to maintain the expected input dimensionality. The hybrid configuration provided a more stringent input-format shift by combining two-channel pretraining with single-channel adaptation. These experiments therefore tested whether continual learning was affected by clinical-domain shift, altered channel semantics or mismatched input dimensionality. Detailed analyses are provided in Supplementary Information S9.2 and S9.5–S9.7.

Neither single-channel nor two-channel processing was uniformly superior during adaptation from D1 to D4 (Extended Data Fig. 2d–f). Single-channel models generally achieved comparable or higher SSIM in the earlier domains and could incorporate datasets lacking complete multimodal acquisitions. Two-channel models more often achieved higher PSNR and lower voxel-wise errors in D3 and D4, with the clearest advantage in tumour imaging. Thus, single-channel processing offered greater flexibility across heterogeneous datasets, whereas genuinely paired inputs could exploit

within-participant anatomical correspondence. This advantage should not be interpreted as a general benefit of multimodal learning in the later domains, where duplicated images preserved dimensionality without providing additional modality information.

We next evaluated the balance between plasticity and retention. Plasticity was measured from performance on the domain immediately after it was learned, whereas retention was assessed by re-evaluating earlier domains after each subsequent adaptation stage. The largest deterioration in previous-domain performance occurred after adaptation to D4 (Extended Data Fig. 3a). In the single-channel configuration, EWC retained PSNR values of only 10.1, 8.3 and 13.2 dB on D1–D3, respectively. By comparison, GBP retained (25.6), (18.5) and 19.3 dB on these domains while achieving 21.4 dB on D4. SEQ showed an intermediate pattern that varied across domains. GBP therefore preserved substantially more previous-domain performance without preventing adaptation to the tumour domain, whereas EWC did not retain earlier reconstruction performance after this pronounced clinical shift.

This ordering was reproduced when the input structure changed and across the evaluated model scales (Extended Data Fig. 4a). Following D4 adaptation, two-channel GBP retained PSNR values of (21.0), (17.1) and 19.9 dB on D1–D3, compared with 11.4, 9.3 and 15.3 dB for EWC. In the hybrid configuration, GBP retained 20.4, 17.2 and 19.9 dB, whereas EWC retained 11.7, 9.5 and 16.1 dB. GBP therefore remained more stable than EWC when adaptation involved either a clinical-domain shift alone or a concurrent change in input format.

Channel configuration also affected the unconstrained and regularized baselines differently (Fig. 2). For SEQ, peak PSNR forgetting decreased from 5.93 dB in the single-channel configuration to 3.00 dB in the two-channel configuration, indicating that channel coupling was associated with greater stability . This association did not extend to EWC, for which peak forgetting increased from 10.20 to 12.13 dB. GBP showed consistently low peak forgetting in the single- and two-channel configurations (0.03 and 0.87 dB, respectively). In the hybrid configuration, GBP similarly achieved $F = 0.87$ dB and BWT $= -0.14$ dB, compared with $F = 11.56$ dB for EWC. Collectively, these results indicate that GBP was less sensitive than the comparator methods to changes in both clinical domain and input structure.

Structural and voxel-wise metrics did not, however, always produce the same ranking (Fig. 2). In the single-channel configuration, SSIM-based ACC was similar for EWC (0.835), SEQ (0.829) and GBP (0.810), but the difference increased in the two-channel configuration, with values of 0.802 for SEQ, 0.782 for EWC and 0.688 for GBP, and was greatest in the hybrid configuration, where GBP achieved 0.616, compared with 0.810 for EWC and 0.802 for SEQ . Because SSIM directly defined the autoencoder reconstruction loss, the higher values achieved by SEQ and EWC may reflect their greater freedom to optimize this loss-aligned structural criterion, whereas blueprint protection imposed an adaptation cost on GBP. This cost was amplified when the two-channel representation was collapsed to one channel, although the present experiments do not isolate the contribution of the channel-collapse adapter. Importantly, GBP showed the lowest forgetting across PSNR, MSE, RMSE and MAE in all three configurations (see Fig. 2). SSIM and the voxel-wise metrics therefore capture complementary properties

of reconstruction, and their combined evaluation indicates that GBP most consistently preserved local intensity fidelity across clinical and input-format shifts, while incurring a structural-similarity cost under two-channel learning and channel collapse. Further analyses are provided in Supplementary Information S9.10.1.

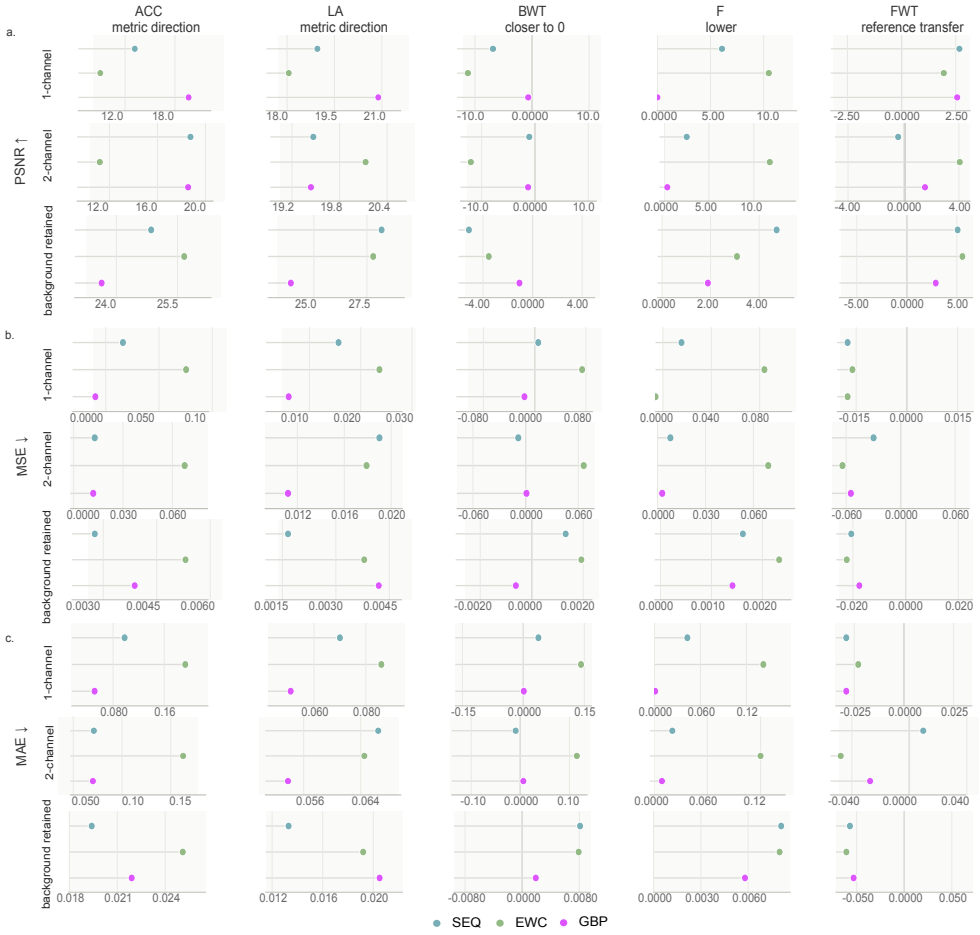


Fig. 2: Continual-learning performance across channel configurations and reconstruction metrics. a–c, Average accuracy after the final stage (ACC), learning accuracy on the just-trained task (LA), backward transfer (BWT), non-negative best-ever peak forgetting ((F)), and forward transfer relative to the independent reference (FWT) for PSNR (**a**), MSE (**b**) and MAE (**c**). Within each panel, rows show the 1-channel, 2-channel and background-retained 1-channel evaluations. Points denote SEQ (blue), EWC (green) and GBP (magenta). Higher values indicate better performance for PSNR, whereas lower values indicate better performance for MSE and MAE; BWT values closer to zero and lower (F) values indicate greater retention. FWT is interpreted relative to the direction and scale of the corresponding image-quality metric. Axis limits vary among metric–score combinations to show differences between methods clearly.

Robustness to background preprocessing

Whole-volume MRI metrics are influenced by the large, relatively invariant background surrounding the brain. Because this region is easier to reconstruct than brain tissue, including it can inflate aggregate image-quality scores and conceal errors within anatomically informative regions. We therefore repeated the single-channel evaluation with background voxels retained to determine whether the principal continual-learning result depended on background preprocessing (Fig. 2).

Retaining the background changed the absolute metric scale and reduced the apparent differences among methods, but GBP continued to show the lowest peak PSNR forgetting. Its F value was 2.04 dB, compared with 3.22 dB for EWC and 4.83 dB for SEQ (Fig. 2). GBP also achieved the backward-transfer value closest to zero BWT $= -0.57$ dB. These results indicate that the relative retention advantage of GBP was present both when the evaluation was restricted to the signal region and when the complete volume was assessed. Additional results are provided in Supplementary Information S9.9.

Background retention nevertheless changed the failure modes visible in the evaluation. With background voxels removed, EWC showed substantial forgetting after D4 adaptation, with BWT $= -10.20$ dB and $F = 10.20$ dB. When the background was included, its performance changed little after the final update, but it also learned D4 poorly: its D4 PSNR was 19.26 dB, compared with 24.45 dB for SEQ and 22.75 dB for GBP. The apparent stability of EWC under this evaluation therefore reflected limited plasticity rather than successful retention combined with adaptation. GBP also incurred an adaptation cost, showing the lowest background-inclusive learning accuracy LA $= 24.34$ dB; nevertheless, it learned the new domain more effectively than EWC while retaining more performance on the earlier domains (Supplementary Information S9.10.2).

Including the background also increased forward-transfer scores and caused SSIM to approach saturation. Background-inclusive SSIM exceeded (0.997) on D2 and D3 for all three methods and did not reveal either the voxel-wise regressions or the limited D4 learning observed with EWC. Signal-region metrics therefore provided the more stringent test of forgetting in brain tissue, whereas background-inclusive metrics characterized reconstruction across the complete image volume. Across both preprocessing regimes, GBP achieved the most consistent balance between retaining earlier-domain performance and adapting to D4. The comparison also reveals the cost of this constraint: protecting the blueprint improved retention but reduced learning accuracy under the background-inclusive evaluation. Further analyses are provided in Supplementary Information S9.10.2.

Clinical adaptation reveals task-dependent representations

Representations optimised for image reconstruction may not transfer equally to generative, diagnostic and prognostic objectives. We therefore examined whether Alcmaeon's pretrained representations retained information relevant to four clinically motivated

downstream tasks: cross-modal synthesis of brain-tumour MRI, adult glioma survival modelling, neurodegenerative-disease classification and postoperative outcome prediction under limited supervision (Figs. 3 and 4; Extended Data Figs. 5 and 6).

For each task, Alcmaeon was compared with established task-specific baselines and available foundation-model representations. We assessed performance using the primary predictive or generative metrics for each endpoint and examined latent-space organisation as a secondary, descriptive analysis. Features were also extracted from the shallower S8-Lv2 and deeper S2-Lv4 configurations to test whether the most informative representation depended on feature depth, modality composition, adaptation strategy and downstream objective. Full benchmarking protocols, statistical comparisons, encoder–generator analyses, survival results and low-shot experiments are provided in Supplementary Information S10.

Cross-modal tumour MRI synthesis

Cross-modal synthesis tests whether a learned representation preserves anatomical correspondence while supporting translation between MRI contrasts. We benchmarked VQVAE [20], AEKL [21], MAISI [22], 3D-SWIN and 3D-SWIN-DiT representations paired with LDM [21], MOTFM [23] and Rectified Flow [24], each of which was adapted to the target translation task (Fig. 3). The 3D-SWIN representation achieved the highest mean fidelity in most translation settings evaluated with these task-adapted generators. When 3D-SWIN-DiT was instead evaluated with its pretrained 3D-DiT generator (the "DiT (Pretrained)" column in Fig. 3a,b), it remained competitive with the alternative latent-space generation strategies. The strongest configurations achieved approximately 28 dB PSNR and SSIM values of (0.93)–(0.94) in the primary tumour cohorts. Performance was more heterogeneous in the external IXI and RHUH-GBM cohorts, although the strongest translations in RHUH-GBM retained PSNR values of approximately 25–27 dB.

These results show that Alcmaeon's representations supported cross-modal translation across several MRI contrasts, while the variation in external cohorts indicates that translation fidelity remained sensitive to cohort composition and acquisition characteristics.

Frozen representations support glioma survival modelling

We tested whether frozen Alcmaeon representations contained prognostic information in a multicentre cohort of 1,551 adults with glioma. Under a shared evaluation protocol, the strongest EWC- and GBP-adapted representations showed similar abilities to rank patients by mortality risk, achieving concordance indices of 0.601 ± 0.016 and 0.601 ± 0.020, respectively. The corresponding values were 0.574 ± 0.013 for ResNet-34, 0.581 ± 0.022 for DUNE U-AE and 0.564 ± 0.010 for HLIP-ViT [3, 25, 26]. The overlapping intervals do not establish superiority between EWC and GBP, but show that GBP retained prognostic information after continual expansion.

GBP and EWC also performed similarly when survival was evaluated at fixed one-, two- and three-year intervals, with AUROCs ranging from 0.719 ± 0.036 to 0.736 ± 0.013 for GBP and from 0.716 ± 0.037 to 0.729 ± 0.013 for EWC. Their relative ordering

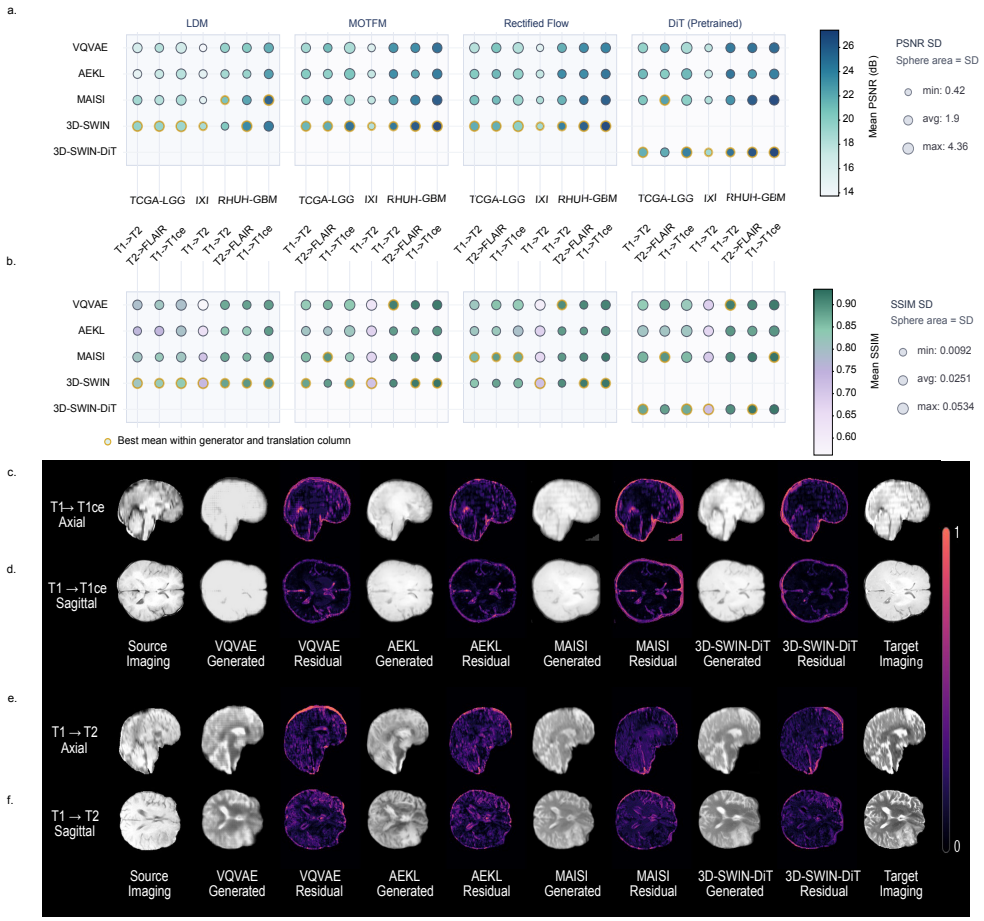


Fig. 3: Clinical adaptation of Alcmaeon across tasks. a. Brain-tumour data generation. Cross-modal MRI translation is evaluated across tumour and external cohorts using PSNR and SSIM matrices for multiple encoder–generator combinations. Qualitative examples and edge-filter visualisations illustrate preservation of anatomical structure and tumour-related image features during synthetic generation.

changed across time points, indicating that neither method was consistently superior for every survival endpoint. Risk groups derived from the Alcmaeon representations showed partial Kaplan–Meier separation, while the corresponding latent-space visualisations provided descriptive evidence of outcome-related organisation (Extended Data Fig. 5).

The analysis also distinguished relative risk ranking from direct prediction of survival time. Among patients with observed deaths, DUNE U-AE and U-VAE achieved mean absolute errors of 510 ± 32 and 502 ± 35 days, respectively, whereas the continual 3D-SWIN-DiT configurations produced larger errors. Alcmaeon therefore retained

information relevant to ranking patients by risk, but accurate estimation of survival time required different representational properties.

Intermediate features support neurodegenerative-disease classification

We examined whether information relevant to Alzheimer's disease classification was retained at different depths of Alcmaeon. Intermediate S8-Lv2 Swin features, combined with a simple classifier, achieved an AUC of 0.845 ± 0.038 and an accuracy of 0.757 ± 0.023. Performance was similar to that of a fivefold CNN baseline (AUC, 0.846 ± 0.033; accuracy, 0.748 ± 0.026) and higher in mean than that of PCA–SVM (AUC, 0.812 ± 0.011; accuracy, 0.716 ± 0.032). With limited labelled data, the AUC increased from 0.528 without task-specific examples to 0.825 ± 0.015 after five-shot adaptation.

We next compared matched continual-learning variants using one-channel S2-Lv4 encoder features. GBP achieved the highest mean accuracy (0.743 ± 0.025) and balanced accuracy (0.737 ± 0.022), compared with accuracies of 0.724 ± 0.035 for SEQ and 0.724 ± 0.036 for EWC. AUCs were similar across GBP (0.820 ± 0.012), SEQ (0.811 ± 0.030) and EWC (0.809 ± 0.022). GBP also achieved the highest mean accuracy in the three-class analysis (0.613 ± 0.034). These differences were modest and do not establish statistical superiority, but indicate that blueprint protection retained disease-related information within the encoder features.

Direct classification using the complete 3D-SWIN-DiT representation remained close to chance for both GBP and EWC in the zero-, one- and three-shot settings (Extended Data Fig. 6). Thus, the accessibility of diagnostic information depended on selecting an appropriate representation depth: intermediate encoder features were more informative for classification than the complete generative representation.

GBP supports postoperative adaptation under limited supervision

Postoperative MRI introduces a substantial anatomical shift from tumour mass to resection cavity, while labelled outcome datasets are often small. We evaluated this setting using paired preoperative and postoperative MRI from 49 patients and compared SEQ, EWC and GBP under the same protocol (Fig. 4). Using intermediate S8-Lv2 features derived from ODI and NDI microstructural maps, GBP achieved an accuracy of 0.7521 ± 0.0553, compared with 0.5938 ± 0.0593 for SEQ and 0.4385 ± 0.0738 for EWC. GBP also achieved the highest F1 score (0.6770 ± 0.0591), with the same ordering observed for sensitivity and precision.

GBP retained this advantage in the low-shot experiments. Its F1 score reached 0.548 ± 0.085 with three-shot adaptation in the S8 D4 configuration and 0.601 ± 0.050 with five-shot adaptation in the L8 D4 configuration, exceeding the corresponding SEQ and EWC results. However, GBP was not uniformly superior, as EWC or SEQ performed better in some fully trained experiments using conventional T1- and T2-weighted MRI. Blueprint protection therefore provided its clearest downstream benefit when adaptation involved limited labels, microstructural imaging or pronounced anatomical change. Given the small cohort, these findings demonstrate comparative

transfer performance rather than clinical validity and require confirmation in larger independent populations.

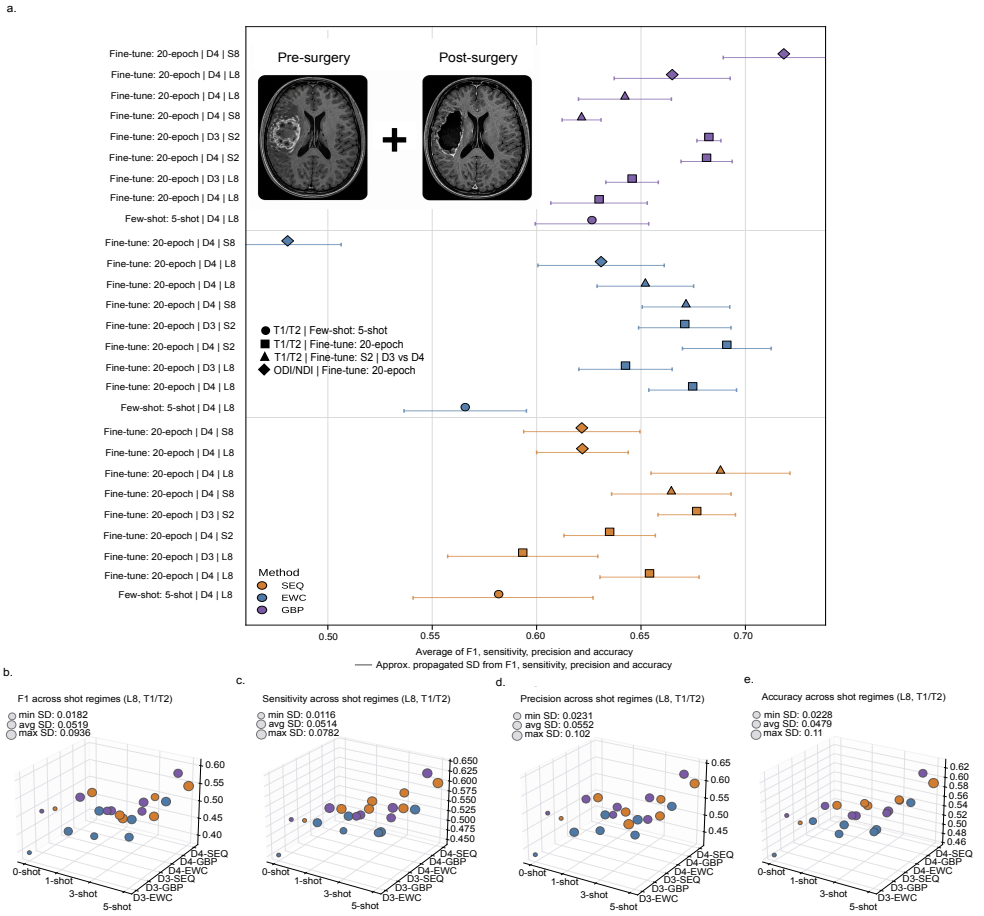


Fig. 4: Clinical adaptation of Alcmaeon across tasks. a. Postoperative brain-tumour outcome prediction. Before- and after-surgery imaging illustrates the anatomical shift from tumour mass to resection cavity, while surrounding performance summaries compare few-shot, chunk-maximum and ODI/NDI transfer settings across SEQ, EWC and GBP. Together, the four panels show that Alcmaeon supports task-specific clinical adaptation for prognostic modelling, disease classification, cross-modal generation and postoperative outcome estimation. The main symbol denotes the balanced mean, computed as the average of F1-score, sensitivity, precision and accuracy. Because all four metrics are derived from the same predictions, covariance terms were not estimated and the propagated s.d. should be interpreted as an approximate visual summary of variability rather than an independent statistical confidence interval.

Together, these benchmarks clarify the complementary contributions of Alcmaeon and GBP. Alcmaeon provides reusable representations from different levels of the model, with each level supporting different applications. Encoder representations, used alone or with the diffusion generator, supported cross-modal image synthesis; intermediate features retained information relevant to neurodegenerative-disease classification; and combined multimodal representations supported glioma risk ranking. GBP helped preserve disease- and prognosis-related information as the model learned new domains, with its clearest downstream advantage observed during postoperative adaptation with limited labelled data and substantial changes in anatomy or imaging modality. When considered alongside GBP's lower forgetting across voxel-level reconstruction measures, these downstream results support GBP as the most suitable of the evaluated adaptation strategies when the main objective is to learn from a substantially different domain while retaining earlier capabilities. However, they do not establish GBP as a universally optimal representation for every downstream task.

Graph-Blueprint Pruning maps structural memory across network modules

Continual-learning methods are typically evaluated by how well they retain performance, but aggregate retention scores do not reveal which parts of a model have been constrained or remain available for subsequent learning. Related masking and subnetwork approaches make parameter allocation explicit [9, 10]. GBP extends this principle by dividing Alcmaeon into predefined computational modules—including attention, feed-forward, normalisation and adaptive-modulation components—and ranking their domain-associated contributions using dataset-aggregated activation–gradient salience. The highest-ranked modules are incorporated into a cumulative blueprint and protected during subsequent adaptation, whereas the remaining modules remain trainable. Separate blueprints are maintained for the 3D-SWIN encoder–decoder and the 3D-DiT latent generator, reflecting their distinct roles in anatomical representation and latent generation (Fig. 5, Extended Data Figs. 7–9 and Methods).

GBP constrained a selective subset of modules rather than freezing the complete architecture. Following sequential adaptation through D4, the number of trainable 3D-DiT modules decreased from 120 to 70, leaving 50 protected and (58.3%) of the predefined modules available for further adaptation. In the 3D-SWIN encoder–decoder, the number of trainable modules decreased from 149 to 86, leaving 63 protected and (57.7%) available. These percentages refer to the number of predefined modules rather than the corresponding proportion of parameters or computational operations, because the modules differ in size. Thus, GBP retained substantial trainable subspaces in both architectural streams while protecting modules selected during earlier domains.

Descriptive comparison of the stage-specific blueprints showed that module selection was distributed across the architecture and that successive domains selected partly distinct combinations of attention, feed-forward, normalisation and modulation components. The cumulative masks distinguish modules that were newly selected, previously protected or still available for adaptation at each stage. They therefore provide an inspectable record of how the hard structural constraint accumulated as the model

progressed through the continual-learning sequence. This record complements the performance-based analysis of the stability–plasticity trade-off by identifying where the constraint was applied within the network.

To examine the anatomical distribution of model sensitivity associated with the modules protected by GBP, we randomly selected one participant from each domain after excluding cases that failed preprocessing or image-quality checks. We then projected the corresponding attribution maps onto anatomical atlases. In the healthy-ageing example, the map conditioned on GBP-protected modules showed a more spatially restricted frontoparietal pattern than the broader medial and posterior distribution obtained from the fully trainable model. In the participant with Parkinson's disease, the protected-module map placed greater emphasis on limbic, thalamic, temporal and midbrain regions. In the developmental example involving an adolescent, attribution was concentrated within selected regions of the default-mode, attention and control networks. In the tumour example, the pattern was concentrated around the opercular, insular and adjacent perisylvian regions. It partly overlapped the lesion and extended into corresponding regions of the contralateral hemisphere that also showed model-derived changes during tumour-image generation. This combined lesion-associated and contralateral pattern was not evident in the attribution map obtained from the fully trainable model.

Because each map was generated from only one randomly selected participant and different anatomical atlases were used across domains, the projections should be interpreted as exploratory visualisations of model sensitivity conditioned on the GBP-protected modules. They do not establish reproducible population-level anatomical patterns, biological circuitry or causal associations. Full regional rankings, comparisons between model components and analyses of the four cases are provided in Fig. 5, Extended Data Figs. 7–9 and Supplementary Information S9.10.

Together, these analyses show that GBP protects modules identified as important to previously learned domains while leaving the remaining modules available for subsequent learning. The blueprints provide an inspectable record of how this structural memory accumulates as new domains are introduced, and the anatomical projections illustrate how the protected modules contribute to model sensitivity across brain regions in individual examples.

Discussion

Alcmaeon addresses a practical limitation of current brain MRI foundation models. Large-scale pretraining can produce reusable representations, but the resulting models are generally treated as fixed systems and adapted separately to each application. Neuroimaging data instead accumulate across populations, diseases, scanners and acquisition protocols. Our findings show that a three-dimensional MRI model trained without manual labels on more than 425,000 volumes and derived imaging maps can be expanded across clinically distinct domains while preserving much of its earlier reconstruction performance. GBP provided the most consistent retention when the

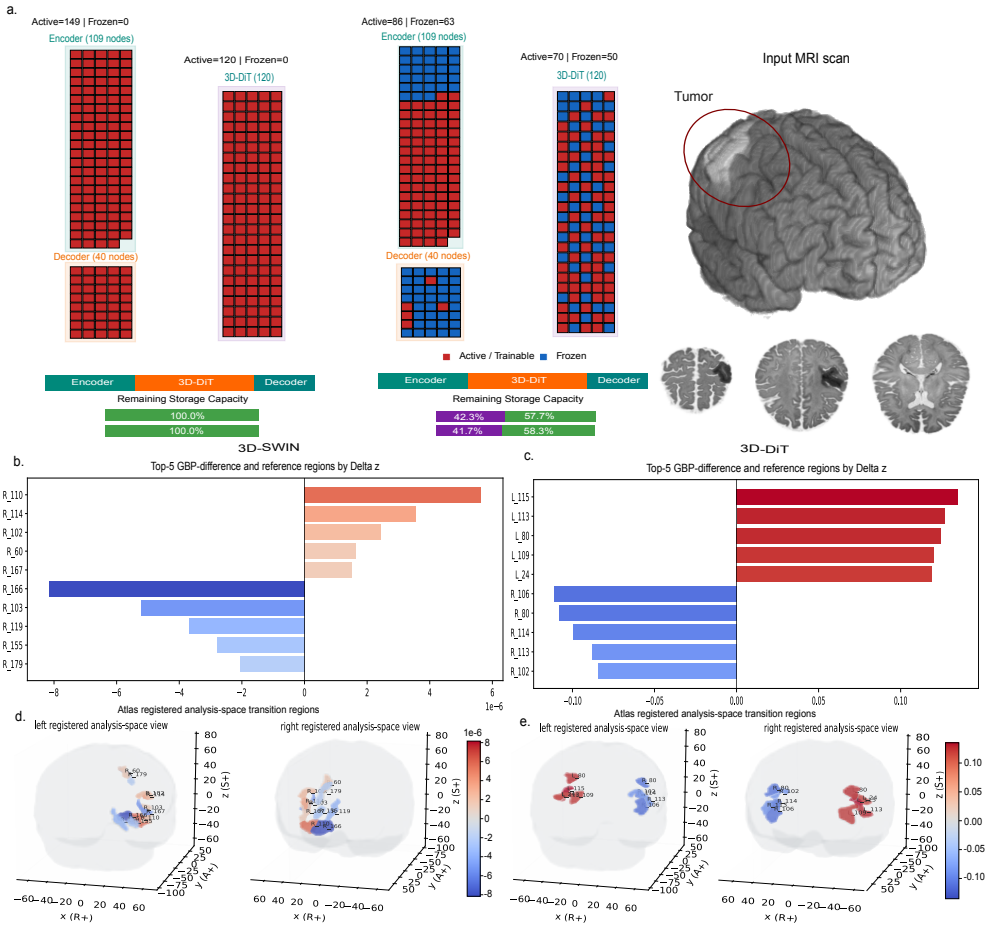


Fig. 5: Graph-Blueprint signatures of capacity allocation and anatomical interpretation during continual neuroimaging adaptation. a–e, Blueprint signatures across the sequential adaptation trajectory. For each domain, GBP ranks task-associated computational modules in the 3D-DiT latent generator and 3D-Swin encoder–decoder, protects the selected modules as structural memory and leaves the remaining modules trainable for subsequent domains. Node grids distinguish protected and trainable modules, and capacity bars show the cumulative fraction of model capacity allocated during adaptation. Ranked blueprint scores illustrate that module selection is structured rather than uniformly distributed. Corresponding latent-space and anatomical projections provide illustrative examples of how the selected computational signatures differ across healthy ageing, neurodegeneration, developmental and psychiatric imaging, and brain tumours. The anatomical projections are based on representative participants and are intended for interpretation of model behaviour rather than population-level neuroanatomical inference.

sequence reached tumour imaging, which introduced the largest anatomical and pathological shift evaluated here. These results support a broader view of foundation models as systems that can continue to learn rather than being pretrained only once.

The pretraining experiments further show that reconstruction quality was not determined by model size alone. Increasing the number of parameters produced modest gains, whereas representation design had a clearer effect. Under the conditions evaluated, deterministic representations achieved higher reconstruction fidelity for structural and diffusion MRI, while variational regularisation benefited some NODDI-derived microstructural maps [19]. Adding the latent 3D-DiT generator had little effect on reconstruction fidelity. The imaging signal, learning objective and latent representation should therefore be considered alongside scale when developing volumetric foundation models.

The principal continual-learning challenge was to retain earlier knowledge while remaining able to learn a new domain. Sequential adaptation and elastic weight consolidation became less reliable after tumour imaging was introduced. GBP instead protected selected modules and restricted subsequent learning to the capacity that remained trainable. This structural constraint limited the loss of earlier-domain performance while allowing adaptation to continue, suggesting that module-level protection may be particularly useful when new data differ substantially in pathology and anatomy. Input structure also formed part of this shift: single-channel models accommodated incomplete multimodal data, whereas paired channels could exploit anatomical correspondence between MRI contrasts. Duplicating an image to maintain a two-channel input preserved dimensionality but added no multimodal information. Evaluation was similarly sensitive to metric choice. SSIM was aligned with the reconstruction objective and approached saturation when background voxels were included, whereas voxel-wise measures were more sensitive to changes within brain tissue. Complementary metrics and anatomically relevant evaluation regions were therefore required to distinguish genuine retention from apparent stability caused by failure to learn the new domain or by the dominance of background voxels.

The downstream benchmarks show that Alcmaeon's value lies not in a single general-purpose representation, but in the complementary information available at different levels of its encoder–diffusion architecture. Encoder features, used alone or with the diffusion generator, supported cross-modal synthesis; intermediate encoder features retained information relevant to neurodegenerative-disease classification; and combined multimodal 3D-SWIN-DiT representations supported glioma risk modelling. These findings also show that reconstruction, generation, classification and prognosis require different representational properties: accurate image synthesis did not guarantee accessible diagnostic information, and effective risk ranking did not ensure accurate prediction of survival time.

In the continual-learning comparisons, GBP was applied to the complete 3D-SWIN-DiT architecture, including both the encoder–decoder and diffusion components, even when downstream analyses subsequently extracted intermediate encoder features. Representations from these GBP-adapted checkpoints retained task-relevant information across diagnostic and prognostic applications after sequential domain expansion. In glioma survival modelling, GBP retained prognostic information and matched the strongest EWC configuration in risk discrimination, although neither approach was consistently superior across all survival endpoints. For Alzheimer's disease classification, intermediate features extracted from the GBP-adapted model achieved the

highest mean accuracy among the matched continual-learning variants, although the differences were modest. GBP showed its clearest mean performance advantage in postoperative prediction, particularly when adaptation involved limited labelled data, diffusion-derived microstructural maps and substantial anatomical change. These results support GBP as a means of preserving transferable information throughout the complete encoder–diffusion model, especially when new domains differ markedly from earlier data. They do not, however, imply that GBP or any single feature level is optimal for every downstream objective.

These benchmarks also suggest directions for future biological and clinical research. Generative models that preserve patient anatomy across MRI contrasts could be developed to produce patient-specific counterfactual references, estimating how the same brain might appear without disease-related changes [27, 28]. The present synthesis experiments provide a technical basis for this possibility but do not validate the generated images as true counterfactuals. Preoperative and postoperative representations could similarly be used to study disease burden, surgical change and prognosis [29, 30], while intermediate representations could support normative modelling and disease-stage inference in neurodegeneration [31, 32]. All of these applications require independent and prospective validation.

The blueprints complement performance evaluation by recording which modules are protected and which remain available for later learning. Like task-specific masking and subnetwork approaches [9, 10], GBP makes this allocation inspectable. The anatomical projections provide exploratory examples of how sensitivity associated with the protected modules is distributed across brain regions. However, each map was generated from only one randomly selected participant, and different atlases were used across domains. The maps therefore cannot establish population-level anatomical patterns, biological circuits or causal associations. Larger studies are needed to determine whether these spatial patterns are reproducible.

These findings demonstrate the potential of structural continual learning for building expandable brain MRI models, while also identifying priorities for further evaluation. We evaluated a single sequence in which tumour imaging was introduced last. Different domain orders may produce different retention patterns and blueprint allocations. Combining cohorts across sites and populations increases diversity but may also allow the model to learn scanner-, site- or population-specific shortcuts, requiring dedicated demographic and site-bias audits. Because GBP protects modules cumulatively, longer learning sequences may eventually leave insufficient capacity for further adaptation and may require mechanisms for sharing, compressing or safely releasing protected capacity. Finally, although the downstream cohorts were independent of pretraining, the clinical analyses were retrospective, and the postoperative evaluation included only 49 participants. Prospective multi-institutional studies, expert clinical assessment and longitudinal validation are therefore required before Alcmaeon can inform patient-level decisions.

In summary, Alcmaeon combines large-scale volumetric pretraining, latent generation and structural continual learning within one brain MRI framework. Its central contribution is not a single representation for every application, but an expandable

set of task-relevant representations coupled to an inspectable mechanism for protecting earlier knowledge. Among the evaluated continual-learning strategies, GBP most consistently retained earlier reconstruction capabilities under pronounced domain shift while preserving features that remained useful for downstream diagnostic and prognostic tasks. These findings provide a foundation for brain MRI models that can incorporate new clinical domains while limiting the loss of previously acquired capabilities.

Online content

Any methods, additional references, source data, extended data, supplementary information, acknowledgements, author contributions and competing interests, and statements of data and code availability are available in the online version of this paper.

Methods

Study design

Alcmaeon was developed as a three-dimensional neuroimaging foundation model for reconstruction, latent generative modelling, continual adaptation and downstream clinical prediction. All models operate on MRI volumes represented as $x \in \mathbb{R}^{B\times C\times H\times W\times D}$, where B is the batch size, C is the number of MRI channels and (H, W, D) are the spatial dimensions. Unless otherwise stated, inputs were trained in either a single-channel setting, in which scans from different modalities were pooled and treated independently, or a two-channel setting, in which paired modalities from the same participant were provided as separate channels. This design allowed the model to operate both on heterogeneous clinical datasets with incomplete imaging protocols and on paired multimodal cohorts.

The methodological framework consists of three components: a Swin-based volumetric autoencoder for self-supervised representation learning [12, 13] , a latent Diffusion Transformer for generative modelling and cross-modal synthesis [15, 17], and a Graph-Blueprint Pruning (GBP) operator for continual learning (The frameworks and their mathematical foundations are described in detail in Supplementary Information S1.–S3.). After pretraining, the learned representations were evaluated on reconstruction, Alzheimer's progression classification, brain-tumour survival estimation, brain-tumour MRI synthesis and post-surgical few-shot outcome prediction (Architectures and fine-tuning strategies are described in detail in Supplementary Information S4.).

Data sources and domain organisation

Alcmaeon was developed using a large-scale collection of three-dimensional MRI data spanning population imaging, neurodegeneration, development, psychiatric variation and adult brain tumours. For self-supervised training, we assembled approximately 425,717 MRI scans from UK Biobank[33, 34], the Parkinson's Progression Markers

Initiative (PPMI)[35], the Alzheimer's Disease Neuroimaging Initiative (ADNI)[36], PREVENT-AD[37], the Adolescent Brain Cognitive Development (ABCD) study[38], Reproducible Brain Charts (RBC)[39], the Harvard Aging Brain Study–Health Disparities (HABS-HD)[40], and multi-institutional adult glioma cohorts. The training data included structural MRI, diffusion-derived maps, NODDI-derived maps, susceptibility-weighted images and standard multiparametric glioma MRI sequences.

The training corpus was organised into sequential domains to evaluate both representation learning and continual adaptation. UK Biobank was used to establish the initial population-scale representation and was subdivided into diffusion MRI, structural MRI and NODDI-derived subsets[33, 34]. Subsequent continual-learning domains comprised D1, healthy-population imaging from HABS-HD[40]; D2, neurodegenerative disease imaging from PPMI, ADNI and PREVENT-AD[35–37]; D3, developmental and lifespan imaging from ABCD and RBC[38, 39]; and D4, adult brain-tumour imaging from UPenn-GBM, UCSF-PDGM and the Erasmus Glioma Database[41–43]. The D4 tumour domain included T1-weighted, contrast-enhanced T1-weighted, T2-weighted and FLAIR MRI and was placed last in the continual-learning sequence to impose a strong pathological distribution shift.

Two complementary input settings were used. In the two-channel setting, paired modalities from the same participant were provided as separate input channels, preserving within-subject correspondence across contrasts. In the single-channel setting, scans from different modalities were pooled and treated independently, enabling training when paired acquisitions were unavailable. This design allowed the model to learn from both paired multimodal datasets and heterogeneous clinical cohorts with incomplete acquisition protocols.

All MRI volumes were processed using a harmonised three-dimensional pipeline. Images were loaded in channel-first format, reoriented to canonical RAS coordinates and resampled to isotropic 1-mm resolution. Structural MRI datasets were spatially normalised to Montreal Neurological Institute space, and skull stripping was performed where required using HD-BET[44]. Intensities were normalised using percentile-based clipping and scaled to the $[0, 1]$ interval. Foreground cropping and resizing were applied to obtain a fixed network input size. For two-channel inputs, the second modality was resampled to the spatial grid of the first modality before concatenation. Stochastic augmentations included random flips along anatomical axes, random 90-degree rotations and intensity perturbations. Each sub-dataset was split into 70% training and 30% validation partitions.

Fine-tuning and downstream evaluation used task-specific clinical cohorts. For Alzheimer's disease progression, we used the BrainLAT dataset[45] and focused on T1-weighted MRI scans with diagnostic labels, defining binary Alzheimer's disease versus healthy-control classification and three-class Alzheimer's disease, frontotemporal dementia and healthy-control classification. The final BrainLAT subset contained 527 subjects. For synthetic MRI generation and cross-modal translation, we evaluated on public brain MRI datasets spanning adult glioma, paediatric high-grade glioma, brain metastases, post-operative glioblastoma and healthy controls, including BraTS-SSA[46], BraTS-MET[47], BraTS-PED[48], TCGA-LGG[49], IXI[50] and

RHUH-GBM[51]. These datasets provided heterogeneous acquisition settings and clinically relevant contrast combinations for testing generative transfer. The downstream test-participants do not overlap with the self-supervised training and adaptation datasets.

For adult brain-tumour survival estimation, we assembled a retrospective multicentre cohort of 1,551 patients with available overall-survival time, event status and multiparametric MRI. The cohort included UPenn-GBM[41], UCSF-PDGM[42], TCGA-LGG/GBM[49, 52], LUMIERE[53], REMBRANDT[54], RHUH-GBM[51], IvyGAP-GBM[55] and CPTAC-GBM[56]. All survival analyses used the same patient list across encoder families, ensuring that 3D-Swin-DiT and comparator models were evaluated on matched imaging and outcome data. For post-surgical outcome prediction, we used the institutional SIND dataset from Addenbrooke's Hospital, comprising paired pre-operative and post-operative T2-weighted MRI scans from 49 patients. Patients were stratified into shorter-term and longer-term survival groups using a 10-month post-operative survival threshold. Together, these downstream cohorts enabled evaluation of Alcmaeon across classification, survival modelling, cross-modal synthesis and few-shot post-surgical adaptation (The pretraining and fine-tuning datasets, strategies and associated information, including demographic and clinical characteristics, are described in detail in Supplementary Information S5.)

Model architecture

The self-supervised reconstruction module, termed 3D-SWIN, is based on a hierarchical shifted-window Swin Transformer encoder–decoder adapted from SwinUNETR. The encoder produces multiscale features across four stages, with patch-merging operations reducing spatial resolution and increasing channel width. The deepest feature map defines the compact latent representation. The decoder reconstructs the volume through learned upsampling and U-Net-style skip connections, preserving multiscale anatomical information. Reconstruction was optimised using structural and voxel-wise fidelity criteria, including SSIM-based loss and standard error metrics.

The latent generative module is a volumetric Diffusion Transformer, termed 3D-DiT. Latent feature maps extracted from the 3D-SWIN bottleneck are tokenised into a voxelised latent grid. A forward diffusion process corrupts the latent with Gaussian noise according to a variance schedule, and the transformer denoiser learns to predict the injected noise at each diffusion step. Diffusion time is encoded with sinusoidal embeddings and injected through adaptive normalisation. At generation, the reverse process iteratively denoises a latent sample, which is devoxelised and decoded by the 3D-SWIN decoder to reconstruct or translate the target MRI volume.

The full 3D-SWIN-DiT architecture couples the deterministic 3D-SWIN with a latent generator operating on the bottleneck representation. The bottleneck generator was implemented either as a variational autoencoder or as the proposed diffusion-only transformer formulation (3D-DiT). Model scale was varied independently of token resolution using Small, Base, Large and Extra-Large backbones, with approximate parameter counts of 33M, 131M, 580M and 676M, respectively. Additional ablations evaluated patch levels, latent hierarchy depth and input-channel configuration.

Self-supervised pretraining

Pretraining was performed by reconstructing the input MRI volume from its latent representation. The 3D-SWIN established the latent anatomical metric, whereas the diffusion module learned the stochastic structure of the latent distribution. For the diffusion objective (3D-DiT), clean latents were noised over 500–1,000 diffusion steps and the denoiser was trained using a simplified denoising score-matching loss between the true and predicted noise. Batch size, spatial resolution and model scale were selected by controlled ablation. Distributed batches of 128–512 produced more stable optimisation than small single-GPU batches, and a batch size of 512 was used for subsequent experiments. Both 64^3 and 128^3 volumes preserved major anatomical and pathological structures, but 128^3 did not provide sufficient downstream improvement to justify the increased cost. Therefore, 64^3 was selected as the operating resolution. Training was implemented in PyTorch and MONAI with automatic mixed precision. The detailed results and hyperparameter analyses for self-supervised training are provided in Supplementary Information S8.

Continual-learning strategies

Continual learning was evaluated across the sequential domains D1–D4. Three strategies were compared. The sequential baseline (SEQ) updated all trainable parameters without an explicit retention mechanism. Elastic Weight Consolidation (EWC; [8]) used a diagonal Fisher approximation to penalise changes in parameters estimated to be important for previous tasks. Graph-Blueprint Pruning replaced soft anchoring with structural preservation of task-relevant computational circuits.

GBP partitions the network into computational units, including attention, feed-forward, normalisation and adaptive-modulation modules. For each probe sample, unit-level salience was estimated using the activation–gradient product, $[s_n(x) = \mathbb{E} * j \left[|a * n, j(x)\partial_{a_{n,j}}\mathcal{L}|\right],]$ where $a_{n,j}$ is the activation of unit n and $\mathcal{L}$ is the task objective. Salience vectors were aggregated across probe samples and compressed by principal component analysis to define a task blueprint. A blueprint score combined mean salience with participation in the dominant salience subspace. At each continual-learning stage, an upper-quantile rule selected salient units among the currently trainable complement, and these units were frozen exactly by masking their optimiser updates. Frozen sets were monotone across tasks, so each new stage operated in a residual trainable subspace of the previous model. Blueprint scores from previous stages were fused by an element-wise extremal rule, ensuring that units salient for any earlier task remained eligible for protection. Separate blueprint streams were maintained for the 3D-SWIN encoder/decoder and the 3D-DiT latent generator. The approach connects mechanistic circuit attribution[57] with subnetwork-preservation continual learning[9, 10]

Blueprint anatomical attribution

To relate GBP capacity allocation to neuroanatomical structure, atlas-based attribution was performed for each continual-learning domain. To preserve realistic anatomical variability, the atlas was aligned to a randomly selected subject from the

corresponding cohort. D1 used a HABS-HD subject and the HCP-MMP1.0–Glasser MNI cortical atlas; D2 used a PPMI subject and the AAL3 anatomical atlas; D3 used an ABCD subject and the Schaefer-400 cortical parcellation with 17-network Yeo ordering; and D4 used an EGD subject and the HCP-MMP1.0–Glasser MNI cortical atlas. Previously derived blueprint files defined all identified nodes, previously frozen nodes and remaining active nodes. For each blueprint scenario, individual modules were perturbed during inference, and the resulting objective was backpropagated to the atlas input to estimate voxel-wise sensitivity. Aggregated gradients produced spatial attribution maps identifying the anatomical or functional regions most dependent on each blueprint-defined circuit subset.

Clinical fine-tuning

For Alzheimer's progression classification, BrainLAT T1-weighted MRI scans were used to define binary and three-class diagnostic tasks involving Alzheimer's disease, frontotemporal dementia and healthy controls. Features extracted from the Swin encoder were normalised at the sample level and standardised using training-set statistics. Classification was performed using support vector machines with radial basis-function kernels and multilayer perceptrons with three hidden layers, batch normalisation, ReLU activations and dropout. Five-fold cross-validation, 70/30 hold-out testing and zero-, one-, three- and five-shot settings were evaluated.

For brain-tumour MRI synthesis, cross-modal translation was evaluated across tumour and external cohorts, including BraTS-SSA, BraTS-MET, BraTS-PED, TCGA-LGG, IXI and RHUH-GBM. Translation tasks included T1→T2, T2→FLAIR and T1→T1ce. Competing autoencoder backbones included VQVAE, AEKL, MAISI and the proposed Swin-based codec. Generative models included latent diffusion, rectified flow and medical optimal-transport flow matching. Models were trained using recommended repository settings where available, with a learning rate of 1×10^{-4}, 200 epochs and a 70/10/20 train/validation/test split.

For adult brain-tumour survival estimation, frozen MRI features were extracted from 3D-SWIN-DiT and compared with MONAI 3D ResNet, DUNE and HLIP encoder families under a common downstream survival protocol. The validation cohort included patients with available overall survival time, event status and skull-stripped T1, T1c, T2 and FLAIR volumes registered to MNI152 space. Each encoder family used its native preprocessing pipeline, but downstream survival modelling was kept identical across feature sets. Survival tasks were evaluated using stratified five-fold cross-validation.

For post-surgical tumour adaptation, pretrained representations were evaluated under few-shot and transfer settings across pre- and post-operative imaging. SEQ, EWC and GBP variants were compared with direct tumour fine-tuning to assess robustness under limited supervision and D4 domain shift.

The detailed experiments and hyperparameter-selection strategies for the four fine-tuning tasks are described in Supplementary Information S7.

Evaluation metrics

Reconstruction and cross-modal generation were evaluated using the structural similarity index measure (SSIM), root mean squared error (RMSE), mean squared error (MSE), mean absolute error (MAE) and peak signal-to-noise ratio (PSNR). Higher SSIM and PSNR indicate better image fidelity, whereas lower RMSE, MSE and MAE indicate lower reconstruction error. Continual learning was evaluated using cross-task matrices in which rows denote the training stage and columns denote the evaluation domain. Average final performance, backward transfer, forward transfer and average forgetting were computed across D1–D4, with sign conventions adjusted for higher-is-better and lower-is-better metrics.

Classification tasks were evaluated using accuracy, balanced accuracy, precision, sensitivity, F1-score and AUROC. Model selection in imbalanced clinical settings was based primarily on F1-score. Survival models were evaluated using concordance for time-to-event discrimination, Kaplan–Meier out-of-fold risk stratification and fixed-horizon AUROC where applicable. For fixed-horizon binary survival tasks, patients censored before the horizon were excluded because their labels were undefined.

The evaluation metrics used across all training and fine-tuning analyses are described in Supplementary Information S6.

Code availability

Code for reproducing the models and analyses will be made publicly available upon publication at https://github.com/ece7048/Alcmaeon, and the trained model weights will be released at https://huggingface.co/ece7048/Alcmaeon. Access can be provided to reviewers upon request.

Data availability

Training cohorts

The data that support the training analyses in this study were obtained from public, controlled-access and institutional neuroimaging resources, as detailed in Supplementary Material S5.1. UK Biobank data were accessed under UK Biobank Application Number 20904. Data from the Parkinson's Progression Markers Initiative (PPMI) were obtained on 25 August 2025 from the PPMI database (https://www.ppmi-info.org/access-dataspecimens/download-data; RRID:SCR_006431). Access to PPMI requires registration and a data-use agreement through the LONI Image and Data Archive (https://ida.loni.usc.edu/home/projectPage.jsp?project=PPMI). Up-to-date information on PPMI is available at https://www.ppmi-info.org. PPMI is a public–private partnership funded by The Michael J. Fox Foundation for Parkinson's Research and its funding partners. ADNI data were accessed through the Alzheimer's Disease Neuroimaging Initiative/LONI portal (https://adni.loni.usc.edu/) and require registration and approval of the ADNI data-use agreement.

The ABCD diffusion-derived data used in this study were obtained from the Fiber Data Hub ABCD release (https://brain.labsolver.org/abcd.html). This resource

provides derived ABCD FIB files, including baseline ($n = 9,713$), 2-year follow-up ($n = 7,199$) and 4-year follow-up ($n = 2,736$) data, under the Creative Commons Attribution–ShareAlike 4.0 International licence. These files are derived diffusion reconstructions rather than raw MRI data; therefore, no additional NDA request was required for the derived FIB files used here. Raw ABCD MRI data, including T1-weighted, diffusion-weighted and SRC.GZ files, remain subject to the National Data Archive data-use agreement and are not redistributed in this study. Additional training resources included the Reproducible Brain Charts dataset (https://reprobrainchart.github.io/docs/datasets/), HABS-HD through LONI (https://ida.loni.usc.edu/home/projectPage.jsp?project=HABS_HD) and PREVENT-AD through the open PREVENT-AD/LORIS portal (https://openpreventad.loris.ca/).

The tumour-domain training data were assembled from multi-institutional glioma MRI cohorts with public, controlled-access or data-use-agreement provenance. These included UPenn-GBM (https://doi.org/10.7937/TCIA.709X-DN49) and UCSF-PDGM (https://doi.org/10.7937/TCIA.BDGF-8V37) from The Cancer Imaging Archive. The Erasmus Glioma Database was accessed through the BMIA XNAT repository (https://xnat.bmia.nl/data/archive/projects/egd) under a custom licence based on CC BY-NC-SA 4.0.

Fine-tuning cohorts

The data that support the fine-tuning analyses were obtained from public, controlled-access and institutional neuroimaging datasets, as detailed in Supplementary Material S5.2. Public and repository-based glioma imaging resources were accessed under their original data-use terms and licences. The generation and translation tasks used BraTS 2025 through Synapse (https://www.synapse.org/Synapse:syn64153130/wiki/630130), TCGA-LGG (https://www.cancerimagingarchive.net/collection/tcga-lgg/) and RHUH-GBM (https://www.cancerimagingarchive.net/collection/rhuh-gbm/).

Public or repository access links for the adult brain-tumour survival cohorts are as follows: UPenn-GBM (https://doi.org/10.7937/TCIA.709X-DN49) TCGA-LGG (https://doi.org/10.7937/K9/TCIA.2016.L4LTD3TK), TCGA-GBM (https://doi.org/10.7937/K9/TCIA.2016.RNYFUYE9), LUMIERE (https://doi.org/10.6084/m9.figshare.c.5904905.v1), REMBRANDT (https://doi.org/10.7937/K9/TCIA.2015.588OZUZB), RHUH-GBM (https://doi.org/10.7937/4545-C905), IvyGAP-GBM (https://doi.org/10.7937/K9/TCIA.2016.XLWAN6NL) and CPTAC-GBM (https://doi.org/10.7937/K9/TCIA.2018.3RJE41Q1). LUMIERE was obtained from Figshare under CC BY 4.0. Across these resources, the available MRI sequences comprised the standard multiparametric glioma protocol: T1-weighted, contrast-enhanced T1-weighted, T2-weighted and FLAIR imaging. The BrainLAT dataset used for Alzheimer's disease and neurodegenerative-disease analyses is publicly available through Synapse (https://www.synapse.org/Synapse:syn51549340/wiki/624187).

The institutional SIND dataset cannot be deposited publicly or released through general request because of participant privacy, governance and data-use restrictions. Scientific collaborations may be considered by contacting S.J.P. (sjp58@cam.ac.uk); or the corresponding author M.M. (mm2703@cam.ac.uk) and responses are expected within approximately two weeks. Any access would require independent institutional

approvals and a formal inter-institutional data-use agreement. Source data supporting the figures are provided with this paper.

Ethics approval and data governance

This study analysed de-identified public, controlled-access and institutional neuroimaging data. For public and controlled-access datasets, participant consent, ethics approval and data governance were obtained by the original studies and repositories. No attempt was made to re-identify participants. Use of controlled-access resources, including UK Biobank, PPMI, ADNI and TCIA/GDC-linked datasets, complied with the access conditions and data-use agreements specified by the original data providers. This research was conducted using the UK Biobank Resource under Application Number 20904. Derived ABCD diffusion files were used from the publicly released Fiber Data Hub resource; raw ABCD MRI data were not redistributed and remain governed by National Data Archive access conditions.

The institutional SIND dataset was used under local governance and data-sharing restrictions and is not available for public redistribution. Any future collaborative access would require independent institutional approvals and a formal data-use agreement. Funding information for the SIND-related work is reported in the Acknowledgements.

0.1 Data preparation of Alzheimer's Disease Neuroimaging Initiative (ADNI)

Data used in the preparation of this article were obtained from the Alzheimer's Disease Neuroimaging Initiative (ADNI) database (adni.loni.usc.edu). The ADNI was launched in 2003 as a public-private partnership, led by Principal Investigator Michael W. Weiner, MD. The original goal of ADNI was to test whether serial magnetic resonance imaging (MRI), positron emission tomography (PET), other biological markers, and clinical and neuropsychological assessment can be combined to measure the progression of mild cognitive impairment (MCI) and early Alzheimer's disease (AD). The current goals include validating biomarkers for clinical trials, improving the generalizability of ADNI data by increasing diversity in the participant cohort, and to provide data concerning the diagnosis and progression of Alzheimer's disease to the scientific community. For up-to-date information, see adni.loni.usc.edu.

Acknowledgment

This work was supported by grants to R.J.G. from the Cancer Research UK (CRUK) Centre, CRUK Children's Brain Tumour Centre of Excellence. This work used, in part, high-performance computing resources awarded to M.M. through UKRI Access to High Performance Computing facilities – autumn 2025, under allocation APP94963, "From MRI to Multi-Omics: An Explainable Foundation Model for Brain Cancer". Computations were performed in part on the Kelvin-2 High Performance Computing Facility, a UK Tier-2 National High Performance Computing facility funded by the

Engineering and Physical Sciences Research Council (EPSRC) and jointly managed by Queen's University Belfast and Ulster University.

All research at the Department of Psychiatry in the University of Cambridge is supported by the NIHR Cambridge Biomedical Research Centre (NIHR203312) and the NIHR Applied Research Collaboration East of England. The views expressed are those of the author(s) and not necessarily those of the NHS, the NIHR or the Department of Health and Social Care. We acknowledge the use of the facilities of the Research Computing Services (RCS) of University of Cambridge, UK. We acknowledge the use of the facilities of the Research Computing Services (RCS) of University of Cambridge, UK. This research has been conducted using the UK Biobank Resource under Application Number 20904.

The work by C.J.M. is part of the grant JDC2023-051807-I funded by MICIU/AEI/10.13039/501100011033 and by ESF+. We thank Rafael Romero-Garcia, Varun Warrier, Clara Pecci Terroba and Marcella Montagnese for their contributions to the curation and preprocessing of the UK Biobank cohort data.

Data used in the preparation of this article were obtained on 25 August 2025 from the Parkinson's Progression Markers Initiative (PPMI) database (https://www.ppmi-info.org/access-dataspecimens/download-data; RRID:SCR_006431). For up-to-date information on the study, see https://www.ppmi-info.org. PPMI is sponsored and partially funded by The Michael J. Fox Foundation for Parkinson's Research, with support from the Aligning Science Across Parkinson's initiative. Additional support is provided by a consortium of industry partners, non-profit organisations and private individuals through financial and in-kind contributions. PPMI partners contribute to the study through the Partner Scientific Advisory Board, which provides feedback on study parameters and supports the evaluation of candidate precision-medicine measures for clinical testing.

Data collection and sharing for the Alzheimer's Disease Neuroimaging Initiative (ADNI) were funded by the National Institute on Aging, National Institutes of Health Grant U19AG024904. The grantee organization is the Northern California Institute for Research and Education. ADNI has also received funding from the National Institute of Biomedical Imaging and Bioengineering, the Canadian Institutes of Health Research and private-sector contributions through the Foundation for the National Institutes of Health (FNIH), including contributions from AbbVie; Alzheimer's Association; Alzheimer's Drug Discovery Foundation; Araclon Biotech; BioClinica, Inc.; Biogen; Bristol-Myers Squibb Company; CereSpir, Inc.; Cogstate; Eisai Inc.; Elan Pharmaceuticals, Inc.; Eli Lilly and Company; EuroImmun; F. Hoffmann-La Roche Ltd and its affiliated company Genentech, Inc.; Fujirebio; GE Healthcare; IXICO Ltd.; Janssen Alzheimer Immunotherapy Research & Development, LLC; Johnson & Johnson Pharmaceutical Research & Development LLC; Lumosity; Lundbeck; Merck & Co., Inc.; Meso Scale Diagnostics, LLC; NeuroRx Research; Neurotrack Technologies; Novartis Pharmaceuticals Corporation; Pfizer Inc.; Piramal Imaging; Servier; Takeda Pharmaceutical Company; and Transition Therapeutics.

Acknowledgement of name inspiration

The foundation model is named Alcmaeon in honour of Alcmaeon of Croton, the ancient Greek natural philosopher and medical theorist of the fifth century BCE. Alcmaeon is widely regarded as a pioneering figure in early biological and medical thought, and is often associated with some of the earliest ideas linking the brain to perception, cognition and human understanding. His originality as a thinker, together with his contributions to anatomy, physiology and early neuroscience, make his name an appropriate inspiration for a model designed to study the human brain across health and disease. Although uncertainties surrounding the chronology of his life have sometimes obscured his historical importance, Alcmaeon remains a foundational figure in the intellectual history of neuroscience.

Supplementary methodological details

Further mathematical, methodological and implementation details are provided in the Supplementary Information. These include the formal problem setting and latent-variable notation; the Swin-Wrap encoder–decoder and hybrid 3D-SWIN-DiT formulation; voxelisation and tokenisation, three-dimensional windowed self-attention, adaptive normalisation and de-voxelisation; the forward and reverse diffusion processes and denoising objective; and the derivations of elastic weight consolidation and Graph-Blueprint Pruning for continual learning. The Supplementary Information also describes dataset organisation, preprocessing and harmonisation, feature-extraction and fine-tuning protocols, optimisation and evaluation procedures, and ablations of model scale, spatial resolution, patch size, hierarchical depth, channel configuration and batch size. Additional sections provide clinical-task-specific methods and benchmarks for neurodegenerative-disease classification, brain-tumour reconstruction and cross-modal generation, and glioma survival modelling, together with few-shot evaluations, latent-space analyses and atlas-based attribution of blueprint-defined circuits. Collectively, these sections provide the mathematical background, step-by-step implementation details and supporting analyses required to reproduce the study while keeping the main Methods focused on the experimental design and core procedures.

Author information

University of Cambridge, Cambridge, UK
Michail Mamalakis, Yonghao Li, Hao Chen, Chao Li, John Suckling, Richard Bethlehem, Stephen J. Price, Pietro Lio
Cancer Research UK Cambridge Institute, University of Cambridge Li Ka Shing Centre, Cambridge, UK
Richard J. Gilbertson, Michail Mamalakis
University of Malaga, Malaga, Spain
Carmen Jimenez-Mesa
University of Virginia, Charlottesville, USA
Antonios Mamalakis

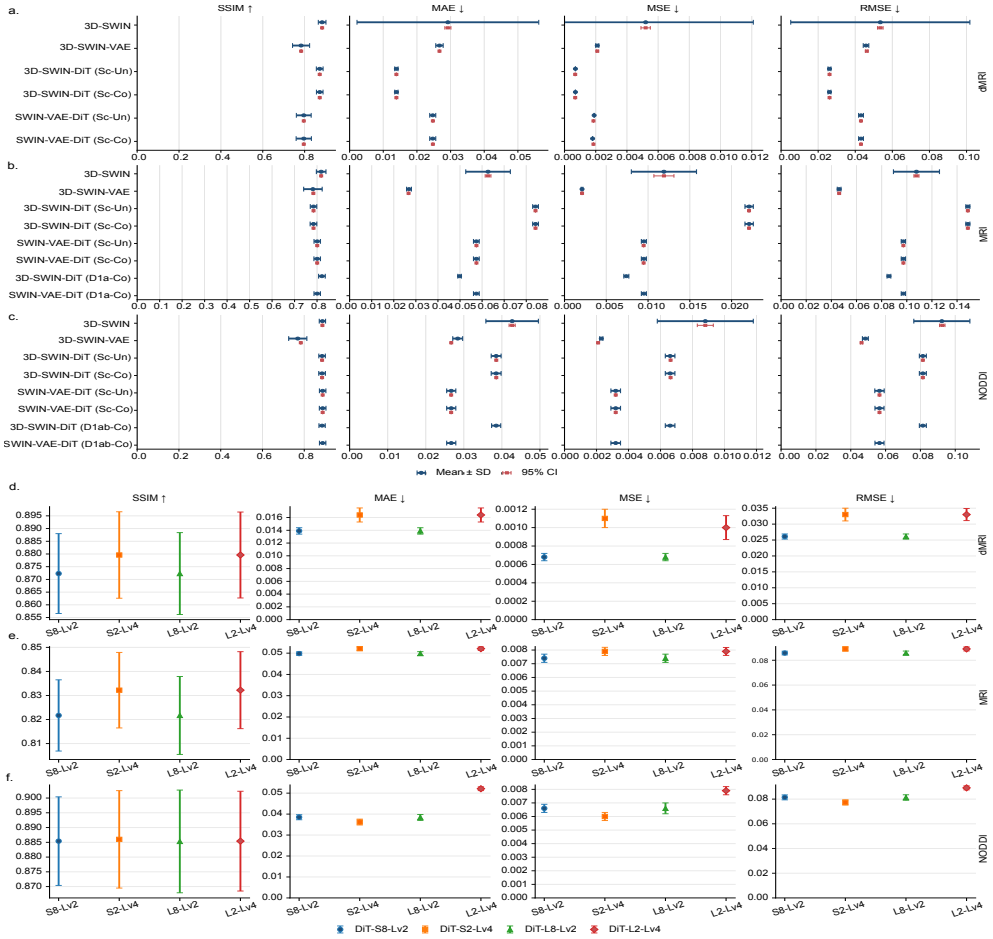
Author contributions

M.M. conceived the study, formulated the Alcmaeon framework, implemented the model architecture, developed the training strategy, designed and implemented Graph-Blueprint Pruning, performed the explainability and interpretability analyses, and supervised the experimental evaluation. M.M. also coordinated the overall analysis, interpreted the results and wrote the first draft of the manuscript. R.B. curated and provided the UK Biobank data and contributed neuroscience feedback throughout the project. J.S. contributed neuroscience guidance and supported the coordination, organisation and storage of the D1–D4 datasets. Y.L. and S.J.P. provided resources and domain expertise for the D4 brain-tumour cohorts and the SIND dataset. Y.L. developed and evaluated the adult brain-tumour survival and fine-tuning pipelines under the supervision of M.M. and S.J.P. C.J. performed the neurodegenerative-disease fine-tuning analyses under the supervision of M.M. and J.S. M.M. and C.J. performed the post-surgical survival fine-tuning and analysis with clinical feedback from S.J.P. H.C. carried out the brain-tumour synthetic generation and cross-modal translation experiments under the supervision of M.M. and C.L. P.L. provided high-performance computing and storage resources. A.M. contributed to the formulation and interpretation of the explainability and interpretability of the foundation model. R.J.G. and S.J.P. provided clinical guidance on brain-tumour tasks, feature importance and interpretation. R.J.G. and P.L. contributed project-management guidance, research-timeline planning and mentorship. All authors contributed to manuscript review and editing.

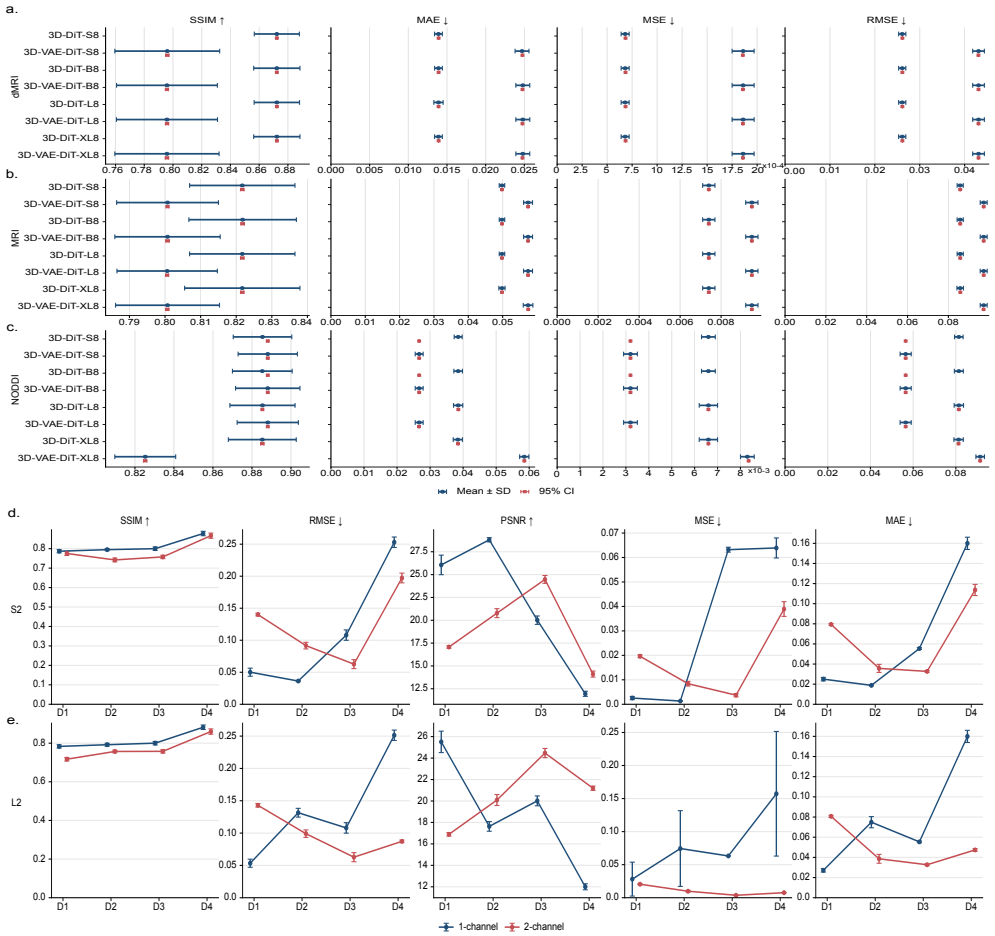
Competing interests

The authors declare no competing interests.

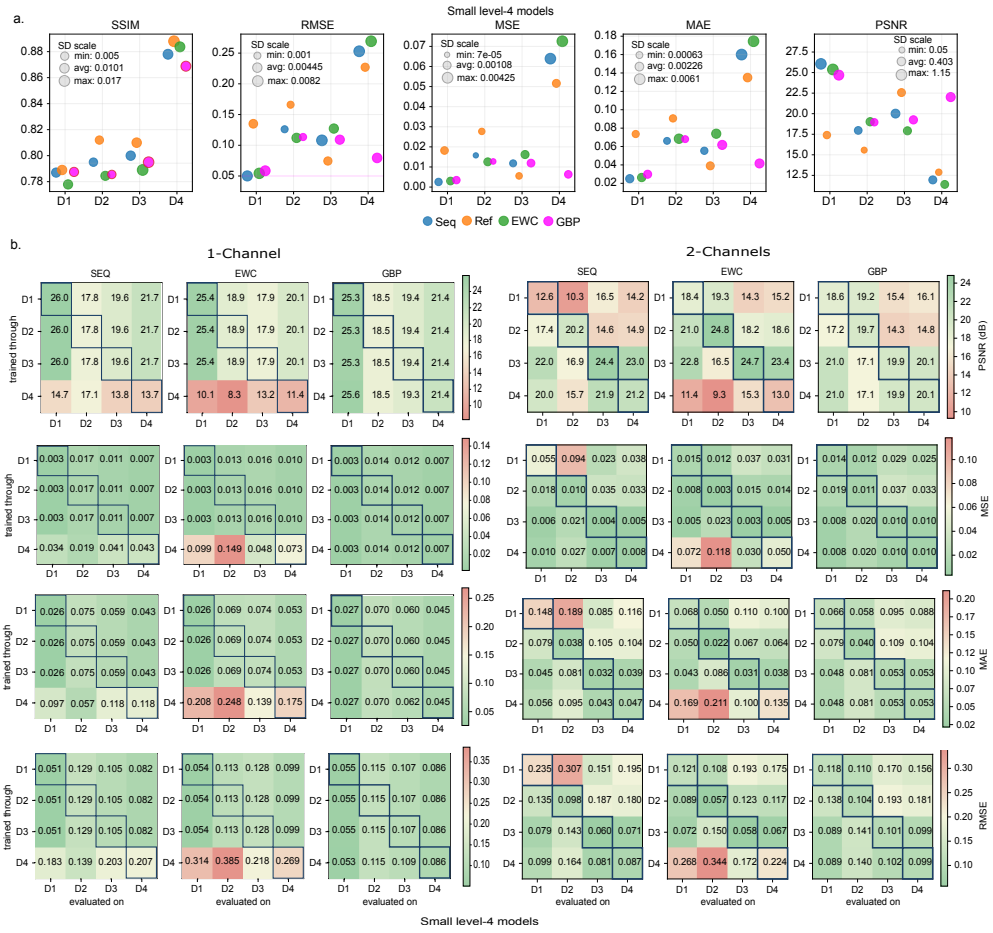
Extended Figures



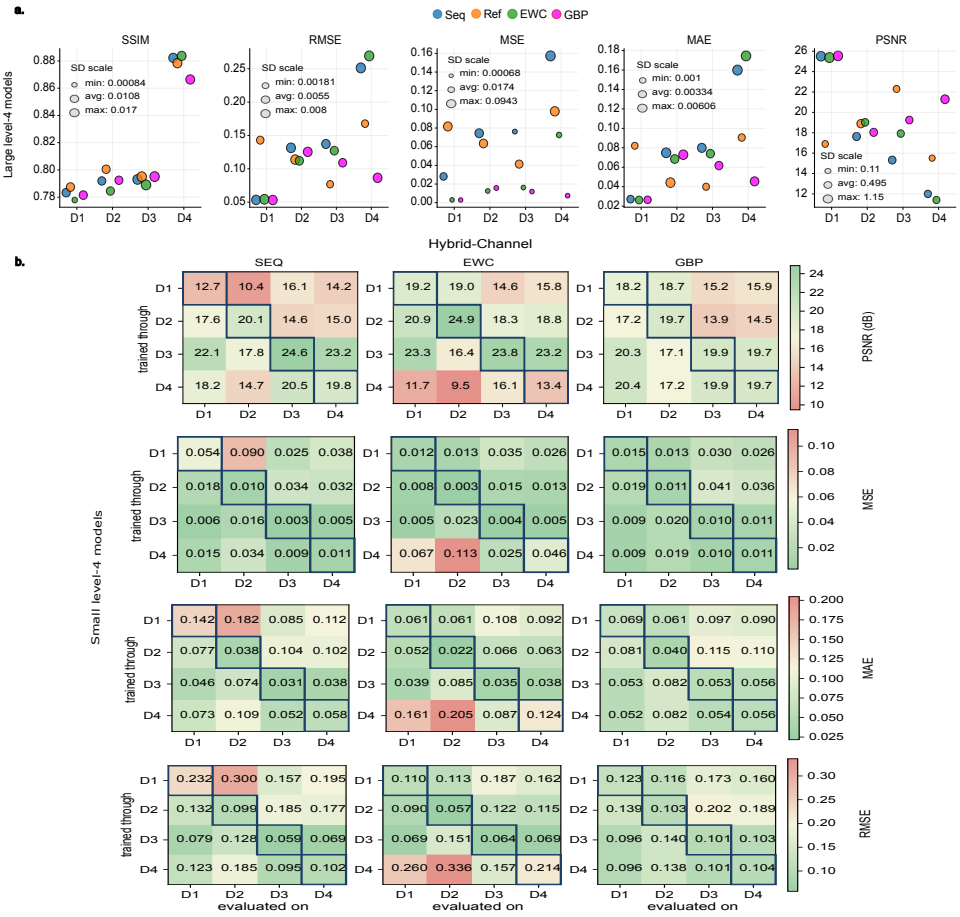
Extended Fig 1: Self-supervised reconstruction and scaling behaviour of 3D-SWIN-DiT. a–c, Reconstruction performance of S8-Lv2 models on UK Biobank diffusion MRI (dMRI; **a**), structural MRI (**b**) and neurite orientation dispersion and density imaging (NODDI; **c**). Deterministic 3D-SWIN and variational 3D-SWIN-VAE models are compared with 3D-SWIN-DiT and SWIN-VAE-DiT diffusion models under the indicated conditioning configurations. Performance is reported using structural similarity (SSIM), mean absolute error (MAE), mean squared error (MSE) and root mean squared error (RMSE). Higher SSIM and lower MAE, MSE and RMSE indicate better reconstruction. Blue intervals denote the mean ± s.d., and red intervals denote the 95% confidence interval where available. **d–f,** Effect of model scale and latent level on reconstruction of dMRI (**d**), structural MRI (**e**) and NODDI (**f**). DiT-S8-Lv2, DiT-S2-Lv4, DiT-L8-Lv2 and DiT-L2-Lv4 models are compared using the same four reconstruction metrics. Sc: training from scratch; Sc-Un: diffusion without conditioning; Sc-Co: diffusion with conditioning; D1a-Co and D1ab-Co denote pretrained diffusion models.



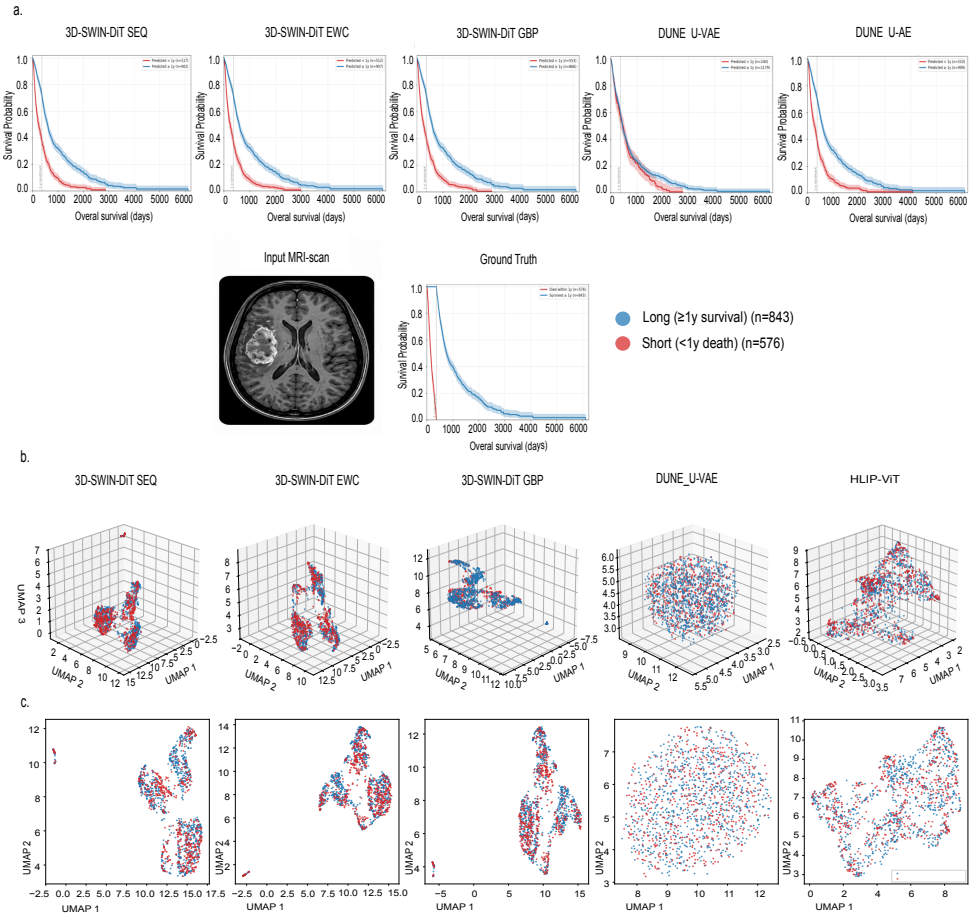
Extended Fig 2: Effects of architecture scale and channel configuration on self-supervised reconstruction. a–c, Reconstruction performance of deterministic 3D-DiT and variational 3D-VAE-DiT models across Small (S8), Base (B8), Large (L8) and Extra-Large (XL8) scales, evaluated on UK Biobank diffusion MRI (dMRI; **a**), structural MRI (**b**) and neurite orientation dispersion and density imaging (NODDI; **c**). Performance is reported using structural similarity (SSIM), mean absolute error (MAE), mean squared error (MSE) and root mean squared error (RMSE). Higher SSIM and lower MAE, MSE and RMSE indicate better reconstruction. Blue intervals denote the mean ± s.d., and red intervals denote the 95% confidence interval. **d,e,** Comparison of one-channel (blue) and two-channel (red) reconstruction using S2 (**d**) and L2 (**e**) models across clinical domains D1–D4. Models are evaluated using SSIM, RMSE, peak signal-to-noise ratio (PSNR), MSE and MAE; higher SSIM and PSNR and lower RMSE, MSE and MAE indicate better performance. The relative advantage of each channel configuration varies across domains: one-channel models perform favourably on D1, whereas two-channel models generally yield lower voxel-wise errors on D3 and D4.



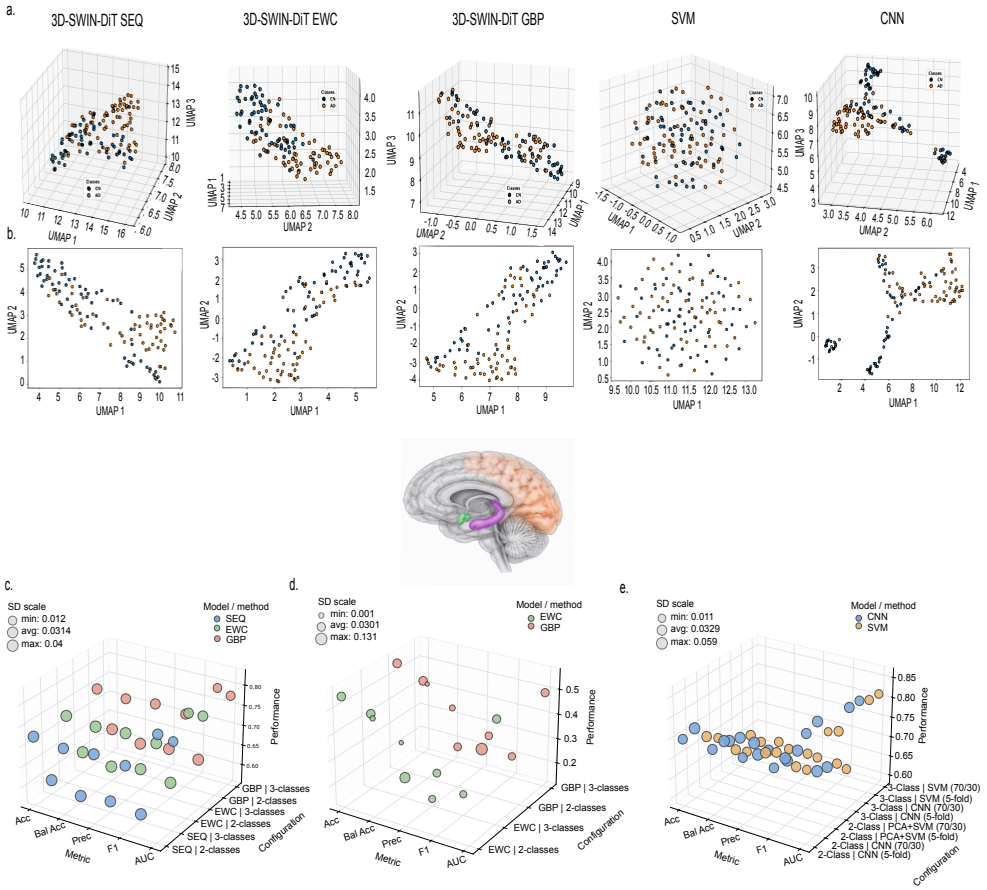
Extended Fig 3: Continual-learning performance across channel configurations. a. Bubble plots compare SEQ, EWC and GBP for single-channel small Lv4 model across SSIM, RMSE, MSE, MAE and PSNR. Bubble size is proportional to the standard deviation; higher SSIM and PSNR indicate better reconstruction, whereas lower RMSE, MSE and MAE indicate lower error. **b.** Cross-task evaluation matrices for one-channel and two-channel models. Rows denote the evaluation dataset and columns denote the sequential training stage. Green shades indicate retained or improved performance, whereas red shades indicate degradation. GBP preserves reconstruction fidelity more consistently than SEQ or EWC, particularly in later domains and under stronger distribution shift.



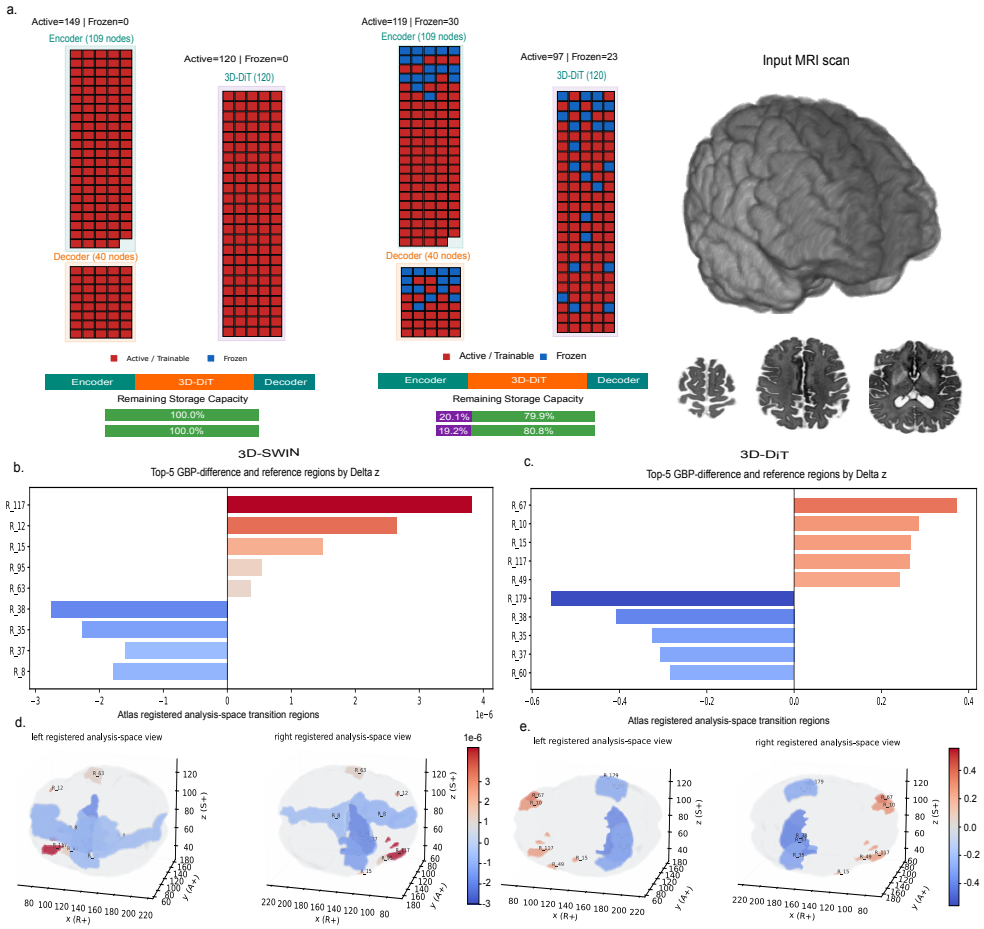
Extended Fig 4: Continual-learning performance across channel configurations. **a.** Bubble plots compare SEQ, EWC and GBP for single-channel large Lv4 models across SSIM, RMSE, MSE, MAE and PSNR. Bubble size is proportional to the standard deviation; higher SSIM and PSNR indicate better reconstruction, whereas lower RMSE, MSE and MAE indicate lower error. **b.** Cross-task evaluation matrices for hybrid-channel model. Rows denote the evaluation dataset and columns denote the sequential training stage. Green shades indicate retained or improved performance, whereas red shades indicate degradation. GBP preserves reconstruction fidelity more consistently than SEQ or EWC, particularly in later domains and under stronger distribution shift.



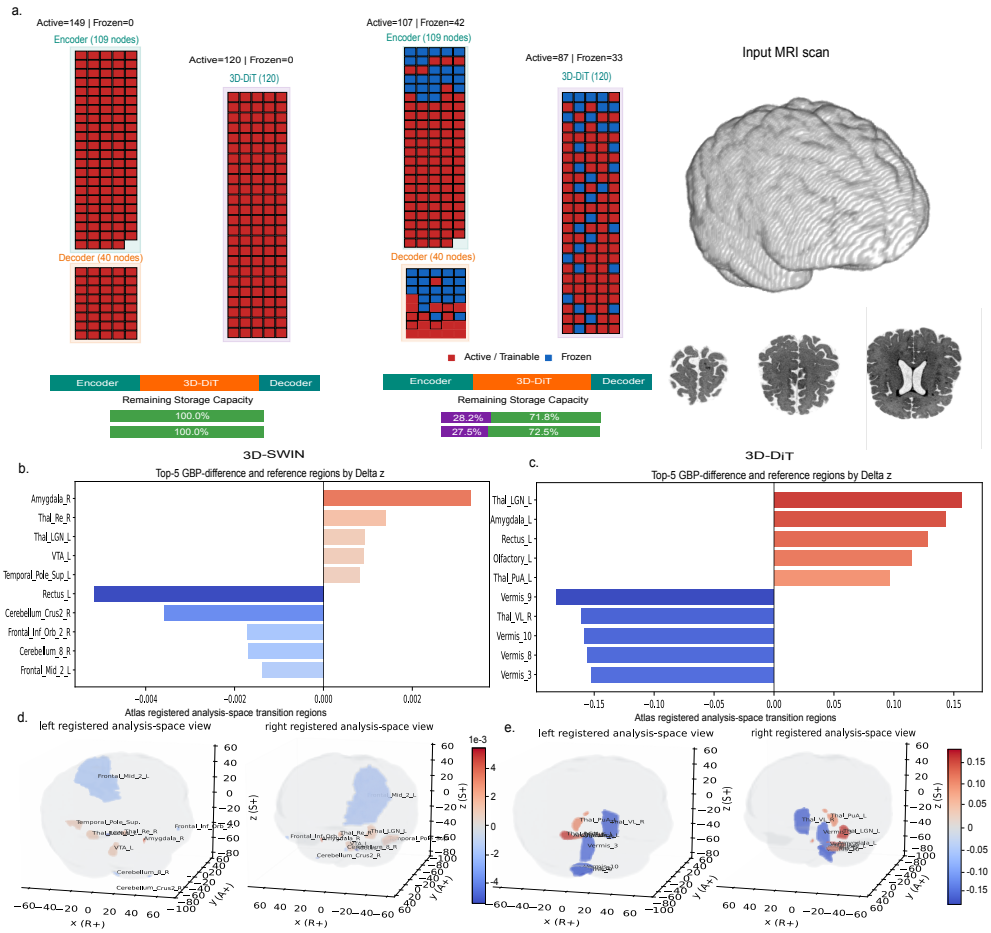
Extended Fig 5: Clinical adaptation of Alcmaeon for adult brain-tumour survival prediction. a, Kaplan–Meier curves derived from out-of-fold predictions of 3D-SWIN-DiT adapted using unconstrained sequential fine-tuning (SEQ), elastic weight consolidation (EWC) or Graph-Blueprint Pruning (GBP), with DUNE U-VAE and DUNE U-AE included as comparison models. Predicted survival distributions are shown for patients with long survival ($\geq$ 1 year; $n = 843$, blue) and short survival ($<$ 1 year; $n = 576$, red), together with the corresponding outcome-defined Kaplan–Meier reference and a representative input MRI scan. Shaded regions indicate uncertainty around the estimated survival curves. **b,** Three-dimensional UMAP projections of PCA-reduced latent features learned by 3D-SWIN-DiT with SEQ, EWC or GBP, compared with DUNE U-VAE and HLIP-ViT. Points represent individual participants and are coloured according to the observed survival group defined in **a**. **c,** Corresponding two-dimensional UMAP projections of the same latent representations, showing the spatial organisation and overlap of short- and long-survival cases. The projections illustrate method-dependent differences in latent-space geometry and in the degree to which survival-related information is organised within the learned representation.



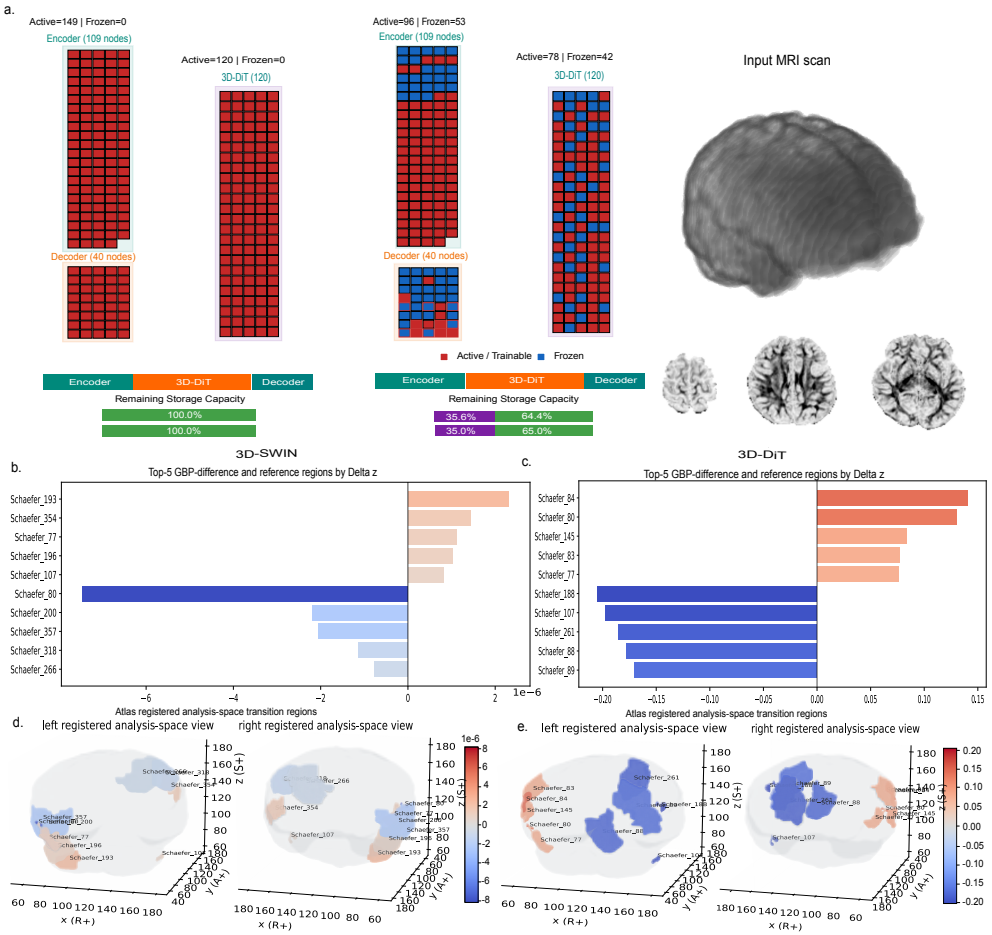
Extended Fig 6: Clinical adaptation of Alcmaeon for modelling Alzheimer's disease progression. a, Three-dimensional UMAP projections of PCA-reduced latent features from one-channel 3D-SWIN-DiT models adapted using unconstrained sequential fine-tuning (SEQ), elastic weight consolidation (EWC) or Graph-Blueprint Pruning (GBP). Conventional support vector machine (SVM) and convolutional neural network (CNN) feature spaces are shown for comparison. Points represent individual participants and are coloured by diagnostic group: cognitively normal (CN), mild cognitive impairment (MCI) or Alzheimer's disease (AD). **b,** Corresponding two-dimensional UMAP projections of the same representations, showing method-dependent differences in the organisation and overlap of the three diagnostic groups. The central brain rendering provides a most common anatomical representation of the regions associated in Alzheimer's disease. **c,** Downstream two-class and three-class classification performance obtained from the one-channel 3D-SWIN-DiT representations learned using SEQ, EWC or GBP. **d,** Corresponding two-class and three-class classification results for the complete 3D-SWIN-DiT configurations adapted using EWC or GBP. **e,** Classification baselines based on SVM and CNN models, including two-class and three-class evaluations using either a 70/30 train–test split or five-fold cross-validation. In **c**–**e**, performance is summarized using accuracy (Acc), balanced accuracy (Bal Acc), precision (Prec), F1 score and area under the receiver-operating-characteristic curve (AUC), together with the corresponding evaluation configuration. Point size represents the s.d. according to the scale shown in each panel.



Extended Fig 7: Graph-Blueprint signatures of capacity allocation and anatomical interpretation during continual neuroimaging adaptation. (a–e) Blueprint maps are shown across the sequential domains D1 healthy population. GBP identifies task-relevant circuits in the 3D-DiT latent generator and 3D-SWIN encoder–decoder, freezes the selected units as structural memory and leaves the remaining units trainable for subsequent adaptation. Active and frozen units are displayed as node grids, with accompanying capacity bars indicating the fraction of preserved and remaining trainable capacity. Ranked blueprint scores identify the most influential units contributing to each domain-specific signature, illustrating that freezing is structured rather than uniformly distributed across the model. The corresponding latent-space and anatomical projections show that blueprint patterns become increasingly domain-specific across the continual-learning trajectory, from more diffuse healthy-population signatures to neurodegenerative, developmental/psychiatric and tumour-associated patterns. Together, these visualisations show that GBP provides both a consolidation mechanism for reducing forgetting and an interpretable structural readout of how Alcmaeon reallocates model capacity across heterogeneous neuroimaging domains.



Extended Fig 8: Graph-Blueprint signatures of capacity allocation and anatomical interpretation during continual neuroimaging adaptation. (a–e) Blueprint maps are shown across the sequential domains D2 neurodegeneration. GBP identifies task-relevant circuits in the 3D-DiT latent generator and 3D-SWIN encoder–decoder, freezes the selected units as structural memory and leaves the remaining units trainable for subsequent adaptation. Active and frozen units are displayed as node grids, with accompanying capacity bars indicating the fraction of preserved and remaining trainable capacity. Ranked blueprint scores identify the most influential units contributing to each domain-specific signature, illustrating that freezing is structured rather than uniformly distributed across the model. The corresponding latent-space and anatomical projections show that blueprint patterns become increasingly domain-specific across the continual-learning trajectory, from more diffuse healthy-population signatures to neurodegenerative, developmental/psychiatric and tumour-associated patterns. Together, these visualisations show that GBP provides both a consolidation mechanism for reducing forgetting and an interpretable structural readout of how Alcmaeon reallocates model capacity across heterogeneous neuroimaging domains.



Extended Fig 9: Graph-Blueprint signatures of capacity allocation and anatomical interpretation during continual neuroimaging adaptation. (a–e) Blueprint maps are shown across the sequential domains D3 developmental/psychiatric cohorts. GBP identifies task-relevant circuits in the 3D-DiT latent generator and 3D-SWIN encoder–decoder, freezes the selected units as structural memory and leaves the remaining units trainable for subsequent adaptation. Active and frozen units are displayed as node grids, with accompanying capacity bars indicating the fraction of preserved and remaining trainable capacity. Ranked blueprint scores identify the most influential units contributing to each domain-specific signature, illustrating that freezing is structured rather than uniformly distributed across the model. The corresponding latent-space and anatomical projections show that blueprint patterns become increasingly domain-specific across the continual-learning trajectory, from more diffuse healthy-population signatures to neurodegenerative, developmental/psychiatric and tumour-associated patterns. Together, these visualisations show that GBP provides both a consolidation mechanism for reducing forgetting and an interpretable structural readout of how Alcmaeon reallocates model capacity across heterogeneous neuroimaging domains.

References

[1] Wald, T. *et al.* *An openmind for 3d medical vision self-supervised learning*, 23839–23879 (2025).

[2] Kaczmarek, E., Szeto, J., Nichyporuk, B. & Arbel, T. Building a general simclr self-supervised foundation model across neurological diseases to advance 3d brain mri diagnoses (2025). URL https://arxiv.org/abs/2509.10620. 2509.10620.

[3] Barba, T. *et al.* DUNE: a versatile neuroimaging encoder captures brain complexity across 3 major diseases: cancer, dementia, and schizophrenia. *GigaScience* **14**, giaf116 (2025). URL https://doi.org/10.1093/gigascience/giaf116.

[4] Tak, D. *et al.* A generalizable foundation model for analysis of human brain MRI. *Nature Neuroscience* **29**, 945–956 (2026).

[5] Wu, Y. *et al.* Braindino: A brain mri foundation model for generalizable clinical representation learning (2026). URL https://arxiv.org/abs/2604.27277. 2604.27277.

[6] van de Ven, G. M., Soures, N. & Kudithipudi, D. in *1.09 - continual learning and catastrophic forgetting* Third edition edn, (ed.Wixted, J.) *Learning and Memory: A Comprehensive Reference (Third Edition)* 153–168 (Academic Press, Oxford, 2025). URL https://www.sciencedirect.com/science/article/pii/B9780443157547000730.

[7] Mirzadeh, S., Farajtabar, M., Görür, D., Pascanu, R. & Ghasemzadeh, H. Linear mode connectivity in multitask and continual learning. *CoRR* **abs/2010.04495** (2020). URL https://arxiv.org/abs/2010.04495.

[8] Kirkpatrick, J. *et al.* Overcoming catastrophic forgetting in neural networks. *Proceedings of the National Academy of Sciences of the United States of America* **114**, 3521–3526 (2017).

[9] Kang, H. *et al.* *Forget-free continual learning with winning subnetworks*, Vol. 162 of *Proceedings of Machine Learning Research*, 10734–10750 (PMLR, 2022). URL https://proceedings.mlr.press/v162/kang22b.html.

[10] Serrà, J., Surís, D., Miron, M. & Karatzoglou, A. *Overcoming catastrophic forgetting with hard attention to the task*, Vol. 80 of *Proceedings of Machine Learning Research*, 4548–4557 (PMLR, 2018). URL https://proceedings.mlr.press/v80/serra18a.html.

[11] Chen, Z. *et al.* *Learning without isolation: Pathway protection for continual learning*, Vol. 267 of *Proceedings of Machine Learning Research*, 9377–9399 (PMLR, 2025).

[12] Liu, Z. *et al.* Swin transformer: Hierarchical vision transformer using shifted windows. *Proceedings of the IEEE/CVF International Conference on Computer Vision (ICCV)* (2021). URL https://arxiv.org/abs/2103.14030.

[13] Tang, Y. *et al.* Self-supervised pretraining of swin transformers for 3d medical image analysis. *Proceedings of the IEEE/CVF Conference on Computer Vision and Pattern Recognition* 20730–20740 (2022).

[14] Çiçek, Ö., Abdulkadir, A., Lienkamp, S. S., Brox, T. & Ronneberger, O. *3d u-net: Learning dense volumetric segmentation from sparse annotation*, Vol. 9901 of *Lecture Notes in Computer Science*, 424–432 (Springer, 2016).

[15] Peebles, W. & Xie, S. *Scalable diffusion models with transformers*, 4195–4205 (2023).

[16] Dosovitskiy, A. *et al.* *An image is worth 16x16 words: Transformers for image recognition at scale* (2021). URL https://openreview.net/forum?id=YicbFdNTTy.

[17] Ho, J., Jain, A. & Abbeel, P. *Denoising diffusion probabilistic models*, Vol. 33, 6840–6851 (2020). URL https://proceedings.neurips.cc/paper/2020/hash/4c5bcfec8584af0d967f1ab10179ca4b-Abstract.html.

[18] Ronneberger, O., Fischer, P. & Brox, T. *U-net: Convolutional networks for biomedical image segmentation*, Vol. 9351 of *Lecture Notes in Computer Science*, 234–241 (Springer, 2015).

[19] Kingma, D. P. & Welling, M. *Auto-encoding variational bayes* (2014). 1312.6114.

[20] Van Den Oord, A., Vinyals, O. *et al.* *Neural discrete representation learning*, Vol. 30 (2017).

[21] Rombach, R., Blattmann, A., Lorenz, D., Esser, P. & Ommer, B. *High-resolution image synthesis with latent diffusion models*, 10684–10695 (2022).

[22] Guo, P. *et al.* *Maisi: Medical ai for synthetic imaging*, 4430–4441 (2025).

[23] Yazdani, M., Medghalchi, Y., Ashrafian, P., Hacihaliloglu, I. & Shahriari, D. *Flow Matching for Medical Image Synthesis: Bridging the Gap Between Speed and Quality* , Vol. LNCS 15975 (Springer Nature Switzerland, 2025).

[24] Liu, X., Gong, C. & Liu, Q. Flow straight and fast: Learning to generate and transfer data with rectified flow. *arXiv preprint arXiv:2209.03003* (2022).

[25] Chen, S., Ma, K. & Zheng, Y. Med3d: Transfer learning for 3d medical image analysis. *arXiv preprint arXiv:1904.00625* (2019). URL https://arxiv.org/abs/1904.00625.

[26] Zhao, C. *et al.* Towards scalable language-image pre-training for 3d medical imaging. *arXiv preprint arXiv:2505.21862* (2025). URL https://arxiv.org/abs/2505.21862.

[27] Sanchez, P., Kascenas, A., Liu, X., O'Neil, A. Q. & Tsaftaris, S. A. *What is healthy? generative counterfactual diffusion for lesion localization*, Vol. 13609 of *Lecture Notes in Computer Science*, 34–44 (Springer, 2022).

[28] Kumar, A. *et al.* *Counterfactual image synthesis for discovery of personalized predictive image markers*, Vol. 13602 of *Lecture Notes in Computer Science*, 113–124 (Springer, 2022).

[29] Pálsson, S. *et al.* Predicting survival of glioblastoma from automatic whole-brain and tumor segmentation of MR images. *Scientific Reports* **12**, 19744 (2022).

[30] Yoon, H. G. *et al.* Multi-parametric deep learning model for prediction of overall survival after postoperative concurrent chemoradiotherapy in glioblastoma patients. *Cancers* **12**, 2284 (2020).

[31] Rutherford, S. *et al.* The normative modeling framework for computational psychiatry. *Nature Protocols* **17**, 1711–1734 (2022).

[32] Young, A. L., Marinescu, R. V., Oxtoby, N. P. *et al.* Uncovering the heterogeneity and temporal complexity of neurodegenerative diseases with subtype and stage inference. *Nature Communications* **9**, 4273 (2018).

[33] Uk biobank. https://www.ukbiobank.ac.uk/.

[34] Sudlow, C., Gallacher, J., Allen, N. *et al.* Uk biobank: an open access resource for identifying the causes of a wide range of complex diseases of middle and old age. *PLoS Medicine* **12**, e1001779 (2015).

[35] Marek, K. *et al.* The parkinson's progression markers initiative (ppmi) – establishing a pd biomarker cohort. *Annals of Clinical and Translational Neurology* **5**, 1460–1477 (2018). URL https://onlinelibrary.wiley.com/doi/abs/10.1002/acn3.644.

[36] Weiner, M. W. *et al.* The alzheimer's disease neuroimaging initiative 3: Continued innovation for clinical trial improvement. *Alzheimer's & Dementia* **13**, 561–571 (2017). URL https://alz-journals.onlinelibrary.wiley.com/doi/abs/10.1016/j.jalz.2016.10.006.

[37] Villeneuve, S. *et al.* The prevent-ad cohort: Accelerating alzheimer's disease research and treatment in canada and beyond. *Alzheimer's & Dementia* **21**, e70653 (2025). URL https://alz-journals.onlinelibrary.wiley.com/doi/abs/10.1002/alz.70653.

[38] Casey, B. *et al.* The adolescent brain cognitive development (abcd) study: Imaging acquisition across 21 sites. *Developmental Cognitive Neuroscience* **32**, 43–54 (2018). URL https://www.sciencedirect.com/science/article/pii/S1878929317301214.

[39] Shafiei, G. *et al.* Reproducible brain charts: An open data resource for mapping brain development and its associations with mental health. *Neuron* **113**, 3758–3779.e6 (2025).

[40] Petersen, M. E. *et al.* Health and aging brain study–health disparities (habs-hd) methods and partner characteristics. *Alzheimer's & Dementia: Translational Research & Clinical Interventions* **11**, e70140 (2025). URL https://alz-journals.onlinelibrary.wiley.com/doi/abs/10.1002/trc2.70140.

[41] The Cancer Imaging Archive. The university of pennsylvania glioblastoma cohort (upenn-gbm) (2021). URL https://doi.org/10.7937/TCIA.709X-DN49. Data set.

[42] The Cancer Imaging Archive. The university of california san francisco preoperative diffuse glioma mri dataset (ucsf-pdgm) (2022). URL https://doi.org/10.7937/TCIA.BDGF-8V37. Data set.

[43] Erasmus MC & Health-RI. The erasmus glioma database (egd) (2021). URL https://xnat.bmia.nl/data/archive/projects/egd. Controlled-access data set.

[44] Isensee, F. *et al.* Automated brain extraction of multisequence mri using artificial neural networks. *Human brain mapping* **40**, 4952–4964 (2019).

[45] Prado, P., Medel, V., Gonzalez-Gomez, R. *et al.* The brainlat project, a multimodal neuroimaging dataset of neurodegeneration from underrepresented backgrounds. *Scientific Data* **10**, 889 (2023). URL https://doi.org/10.1038/s41597-023-02806-8.

[46] Adewole, M. *et al.* The brain tumor segmentation (brats) challenge 2023: Glioma segmentation in sub-saharan africa patient population (brats-africa). *arXiv preprint arXiv:2305.19369* (2023).

[47] Moawad, A. W. *et al.* The brain tumor segmentation-metastases (brats-mets) challenge 2023: Brain metastasis segmentation on pre-treatment mri. *arXiv preprint arXiv:2306.00838* (2023).

[48] Kazerooni, A. F. *et al.* The brain tumor segmentation (brats) challenge 2023: Focus on pediatrics (cbtn-connect-dipgr-asnr-miccai brats-peds). *arXiv preprint arXiv:2305.17033* (2023).

[49] Pedano, N. *et al.* The cancer genome atlas low grade glioma collection (tcga-lgg) (2016). URL https://doi.org/10.7937/K9/TCIA.2016.L4LTD3TK. Data set.

[50] Biomedical Image Analysis Group, Imperial College London. Ixi dataset: Information extraction from images (2002). URL https://brain-development.org/ixi-dataset/. EPSRC GR/S21533/02.

[51] Cepeda, S. *et al.* The río hortega university hospital glioblastoma dataset: A comprehensive collection of preoperative, early postoperative and recurrence mri scans (rhuh-gbm) (2023). URL https://doi.org/10.7937/4545-c905. Data set.

[52] The Cancer Imaging Archive. The cancer genome atlas glioblastoma multiforme collection (tcga-gbm) (2016). URL https://doi.org/10.7937/K9/TCIA.2016.RNYFUYE9. Data set.

[53] Suter, Y. *et al.* The lumiere dataset: Longitudinal glioblastoma mri with expert rano evaluation (2022). URL https://doi.org/10.6084/m9.figshare.c.5904905.v1. Data set.

[54] Scarpace, L., Flanders, A. E., Jain, R., Mikkelsen, T. & Andrews, D. W. Data from REMBRANDT (2019). URL https://doi.org/10.7937/K9/TCIA.2015.588OZUZB. Data set.

[55] The Cancer Imaging Archive. Ivy glioblastoma atlas project collection (ivygap-gbm) (2016). URL https://doi.org/10.7937/K9/TCIA.2016.XLWAN6NL. Data set.

[56] National Cancer Institute Clinical Proteomic Tumor Analysis Consortium. The clinical proteomic tumor analysis consortium glioblastoma multiforme collection (cptac-gbm) (2018). URL https://doi.org/10.7937/K9/TCIA.2018.3RJE41Q1. Data set.

[57] Lindsey, J. *et al.* On the biology of a large language model. *Transformer Circuits Thread* (2025). URL https://transformer-circuits.pub/2025/attribution-graphs/biology.html.